

Herschel Observations of Protoplanetary Disks in Lynds 1641

Sierra L. Grant¹, Catherine C. Espaillat¹, S. Thomas Megeath², Nuria Calvet³, William J. Fischer⁴, Christopher J. Miller³, Kyoung Hee Kim⁵, Amelia M. Stutz^{6,7}, Álvaro Ribas¹, Connor E. Robinson¹

ABSTRACT

We analyze *Herschel Space Observatory* observations of 104 young stellar objects with protoplanetary disks in the ~ 1.5 Myr star-forming region Lynds 1641 (L1641) within the Orion A Molecular Cloud. We present spectral energy distributions from the optical to the far-infrared including new photometry from the *Herschel* Photodetector Array Camera and Spectrometer (PACS) at $70\ \mu\text{m}$. Our sample, taken as part of the *Herschel* Orion Protostar Survey, contains 24 transitional disks, eight of which we identify for the first time in this work. We analyze the full disks with irradiated accretion disk models to infer dust settling properties. Using forward modeling to reproduce the observed $n_{K_S-[70]}$ index for the full disk sample, we find the observed disk indices are consistent with models that have depletion of dust in the upper layers of the disk relative to the midplane, indicating significant dust settling. We perform the same analysis on full disks in Taurus with *Herschel* data and find that Taurus is slightly more evolved, although both samples show signs of dust settling. These results add to the growing literature that significant dust evolution can occur in disks by ~ 1.5 Myr.

Subject headings: Infrared: stars — protoplanetary disks — accretion disks — circumstellar matter

1. Introduction

Protoplanetary disks are composed of gas and dust and are formed in the collapse of a slowly rotating, dense core in the star’s natal, molecular cloud (Terebey et al. 1984). The details of how these disks evolve from initially well-mixed distributions of gas and dust to systems composed

mostly of rocky planets and gas giants are not well understood. As the disk evolves, the dust grains will settle to the midplane where they will grow and the gas will dissipate (e.g., Goldreich & Ward 1973; Weidenschilling 1980; D’Alessio et al. 2006; Testi et al. 2014). Many complex processes occur between the initial formation of the disk and the dissipation of gas, including photoevaporation from the central source, grain growth and settling to the midplane, disk instabilities, sculpting due to companions, and planet formation (e.g., Marsh & Mahoney 1992; Clarke et al. 2001; Dullemond & Dominik 2005; Lubow & D’Angelo 2006; Chiang & Murray-Clay 2007; Alexander et al. 2014; Rosotti et al. 2016; Pinilla et al. 2017; Armitage 2018; Hendl et al. 2018; van der Marel et al. 2018).

We can use spectral energy distributions (SEDs) of young objects and their circumstellar disks to analyze these systems and constrain their properties. The circumstellar material is irradiated by the central star and re-emits radiation primar-

¹Department of Astronomy, Boston University, 725 Commonwealth Avenue, Boston, MA 02215, USA

²Ritter Astrophysical Research Center, Department of Physics and Astronomy, University of Toledo, Toledo, OH 43606, USA

³Department of Astronomy, University of Michigan, Ann Arbor, MI 48109, USA

⁴Space Telescope Science Institute, Baltimore, MD 21218, USA

⁵Department of Earth Science Education, Kongju National University, 56 Gongjudaehak-ro, Gongju-si, Chungcheongnam-do 32588, Republic of Korea

⁶Departamento de Astronomía, Universidad de Concepción, Casilla 160-C, Concepción, Chile

⁷Max-Planck-Institute for Astronomy, Königstuhl 17, 69117 Heidelberg, Germany

ily at infrared and millimeter wavelengths (e.g., Kenyon & Hartmann 1987; Calvet et al. 1992; Chiang & Goldreich 1997; Calvet & Gullbring 1998; D’Alessio et al. 1999, 2001, 2006; McClure et al. 2013a; Ingleby et al. 2013). In particular, spectral indices of the disk emission can be used to study some of its properties; these indices are defined as

$$n_{\lambda_1-\lambda_2} = \frac{\log(\lambda_2 F_{\lambda_2}) - \log(\lambda_1 F_{\lambda_1})}{\log(\lambda_2) - \log(\lambda_1)}, \quad (1)$$

which are essentially slopes between λ_1 and λ_2 . These indices can distinguish evolutionary stages, especially when used in the NIR to mid-infrared (MIR; e.g., Adams et al. 1987; Lada 1987; Andre & Montmerle 1994; Calvet et al. 1994; Greene et al. 1994; Evans et al. 2009; Dunham et al. 2014; Kryukova et al. 2014; Furlan et al. 2016). In this paper, we adopt the criteria of Furlan et al. (2016) and Kryukova et al. (2014), where Class 0/I protostars have $n_{[4.5]-[24]} > 0.3$, flat-spectrum objects have $-0.3 < n_{[4.5]-[24]} < 0.3$, and Class II objects (i.e., a pre-main sequence star surrounded by a disk) have $-1.6 < n_{[4.5]-[24]} < -0.3$. We can also use spectral indices to infer disk properties, such as gaps, dust settling, and truncation (e.g., McClure et al. 2010; Manoj et al. 2011; Furlan et al. 2011; Maucó et al. 2016).

The large size and relatively close proximity of the Orion Molecular Cloud complex makes it an ideal region to study active star formation. These clouds, which span roughly 90 pc in length (Megeath et al. 2012), are at a distance of ~ 400 pc (Kounkel et al. 2017). Kounkel et al. (2017) find the Orion Nebula Cluster lies at 388 ± 5 pc and the southern portion of Lynds 1641 (L1641) is located at 428 ± 10 pc. The Orion Molecular Cloud complex houses regions of both high-mass and low-mass star formation in a relatively dense area. The complex is composed of two clouds, A and B. Cloud A contains the Orion Nebula Cluster to the north, with low-mass and high-mass star formation in its dense center, and L1641 to the south with a large population of low-mass stars (e.g., Megeath et al. 2016). L1641 has been estimated to have over 1600 Class II and Class III (i.e., pre-main sequence stars without disks) objects (Hsu et al. 2012; Pillitteri et al. 2013) with an age of 1–3 Myr (e.g., Gálfalk & Olofsson 2008; Fang et al. 2009, 2013; Hsu et al. 2012). L1641

contains a population of young stars comparable in size to the Orion Nebula Cluster, but due to its lower spatial density and lack of O stars, it has a much lower infrared background and a lower degree of source confusion. This makes it ideal for sampling spectral energy distributions in the infrared with the modest angular resolution of the *Spitzer Space Telescope* and *Herschel Space Observatory*. L1641 is undergoing more active star formation than Taurus and other nearby star-forming regions and provides us with a large sample of targets that span the first phases of evolution while having roughly the same age and initial chemical composition (e.g., Megeath et al. 2016).

We present *Herschel Space Observatory*⁸ (Pilbratt et al. 2010) photometry taken with the Photodetector Array Camera and Spectrometer (PACS; Poglitsch et al. 2010) of 104 Class II objects in L1641. These protoplanetary disks were observed as part of the *Herschel* Orion Protostar Survey (HOPS), an open-time key program (e.g., Manoj et al. 2013; Stutz et al. 2013; Furlan et al. 2016; Fischer et al. 2017; B. Ali et al. 2018, submitted). We include ancillary data from the literature to construct dereddened 0.55–70 μm SEDs for 98 targets. We use a forward modeling process to compare the D’Alessio et al. (1998, 1999, 2001, 2006) self-consistent, irradiated, accretion disk models to our full disk sample indices. We also perform this forward modeling analysis on a sample of Class II objects in Taurus with PACS data from Howard et al. (2013) to put our sample into context with a more well-studied region.

In Section 2, we present the *Herschel* observations and the reduction procedures used to obtain photometry. In Section 3, we analyze the disk properties of the sample, including a description of the stellar sample, presentation of SEDs of individual objects and the median SED for the sample (as well as the full disks and transitional disks separately), and disk classification. In Section 4, we compare our full disk sample with irradiated disk models. We discuss our findings in Section 5 and summarize this work in Section 6.

⁸*Herschel* is an ESA space observatory with science instruments provided by European-led Principal Investigator consortia and with important participation from NASA.

2. Observations

We compiled an initial sample of young stellar objects (YSOs) on the basis that they were classified as Class II objects in Megeath et al. (2012, 2016) and were located in L1641 (we require that our sample be located below -6° declination, see Figure 1). For this sample, we extracted photometry from the *Herschel* Orion Protostar Survey (HOPS) open-time key program in 2010 and 2011 (e.g., Manoj et al. 2013; Stutz et al. 2013; Furlan et al. 2016; Fischer et al. 2017; B. Ali et al. 2018, submitted). We note that Megeath et al. (2012) used *Spitzer* Infrared Array Camera (IRAC, Fazio et al. 2004) and Multiband Imaging Photometer for SIRTF (MIPS, Rieke et al. 2004) observations. There are an additional 11 sources that were reclassified from Class II objects to Class 0/I/flat-spectrum sources using the *Herschel* observations and they are presented in Furlan et al. (2016); we do not include them here. Removing these objects results in a reduced sample of 169 objects out of the 180 Class II L1641 objects in Megeath et al. (2012) for which we extracted photometry with the HOPS maps. (We discuss further reducing our analysis sample to 104 objects in Section 3.1.)

The HOPS maps are square maps of 5 or 8 arcmin on a side that were optimized to detect *Spitzer*-identified protostars with expected $70\ \mu\text{m}$ flux densities greater than 42 mJy. Each field was scanned and then cross-scanned in the orthogonal direction to reduce noise. The presence of Class II sources was serendipitous.

The maps used for point-source photometry were reduced with a high-pass filtering method that reduces the contribution of smoothly varying extended structure while preserving the integrity of point sources. This process is described in detail by B. Ali et al. 2018, submitted. We obtained photometry for each source in a circular aperture of 9.6 arcsec in radius with background subtraction of the signal measured in an annulus extending from 9.6 to 19.2 arcsec. These aperture parameters are not much larger than the $70\ \mu\text{m}$ angular resolution of PACS (5.2 arcsec) in order to reduce the influence of the bright, spatially varying nebular emission in Orion. The resulting values were divided by 0.7331 to account for flux in the wings of the point-spread function that is not included in the aperture. The uncertainty for each measure-

ment is dominated by a 5% floor that was included to account for the global calibration uncertainty. The data were processed with version 9 of the *Herschel* Interactive Processing Environment, using the FM7 version of the PACS calibration. The *Herschel* fluxes are listed in Table 1 and Table 7. Table 1 contains objects included in our analysis and Table 7 contains objects that were removed from the sample as described in Section 3.1.

3. Observed Properties

3.1. Stellar Sample

L1641 is a relatively well-studied region, and the works of Fang et al. (2009, 2013), Hsu et al. (2012), Caratti o Garatti et al. (2012), and Kim et al. (2013, 2016) provide stellar properties for a subset of its YSO population. Gálfaik & Olofsson (2008) derive an age of ~ 1 Myr for region. Fang et al. (2013) found similar median ages, with 1.5 Myr for the “clustered” YSOs and 1.6 Myr for the “isolated” YSOs. We adopt 1.5 Myr for our analysis.⁹

From the 169 Class II objects discussed in Section 2, we remove objects that meet any of the following criteria: 1) their *Herschel* maps show nearby close sources or nebulosity; 49 are flagged for this reason. 2) They have visual extinctions, A_V , equal to or greater than 15; this applies to 18 systems. 3) They have colors uncharacteristic of classical T Tauri stars (CTTSs); this applies to one object. Including the targets with nearby sources or nebulosity would make the $70\ \mu\text{m}$ fluxes for those objects more uncertain due to contamination, thus making our analysis using the $70\ \mu\text{m}$ data unreliable. Objects with $A_V \geq 15$ will have higher uncertainties and we remove them to avoid introducing biases. The one source that does not have colors characteristic of a CTTS is an A star and should not be compared directly to the rest of the sample. We present the *Herschel* photometry

⁹Our sources were observed in fields chosen to target protostars, so we expect that our sources are associated with dense gas filaments/clumps and are similar in age to the “clustered” age found by Fang et al. (2013). Additionally, the derived age depends on the chosen pre-main-sequence track. Fang et al. (2013) used the Dotter et al. (2008) isochrones while Hsu et al. (2012) find an age of 3 Myr using the Siess et al. (2000) and Baraffe et al. (1998) isochrones. We note that age differences in the literature will not significantly impact our results.

and stellar properties for these flagged objects in the Appendix, but these objects are not included in the rest of the analysis. The 104 protoplanetary systems analyzed in this work are marked in the L1641 column density map shown in Figure 1 (Stutz & Kainulainen 2015; Stutz & Gould 2016).

For our sample of 104 systems, we obtained literature values of spectral types for 75 objects, A_V values for 98 objects, luminosities (L) for 77 objects, and mass accretion rates (\dot{M}) for 61 objects. These values and their references are listed in Table 2. More than 75% of the spectral types in this sample come from Hsu et al. (2012) using the Hernández et al. (2004) spectral-typing process, with typical uncertainties of less than one subclass. The median spectral type for the sample is M1 (Figure 2). Additionally, for the flagged sample we have spectral types for 31, A_V values for 59, luminosities for 40, and mass accretion rates for 24 objects. These values are available in Table 8 in the Appendix.

Of the 98 A_V determinations, 77 were obtained from the literature (see the Appendix for the flagged sample). The rest of the A_V determinations were calculated in this work using the observed J , H , and K_S photometry bands from the Two Micron All-Sky Survey (2MASS, Skrutskie et al. 2006), the Mathis (1990) reddening law (with an $R_V = 3.1$; the extinction curve in the JHK -bands is similar for the McClure 2009 law and we adopt $A_H/A_J = 0.624$ and $A_K/A_J = 0.382$), and by calculating the intrinsic color from the CTTS locus from Meyer et al. (1997),

$$(J-H)_{\text{CTTS}} = 0.58 \pm 0.11(H-K_S)_{\text{CTTS}} + 0.52 \pm 0.06, \quad (2)$$

after converting the locus to the 2MASS photometric system using conversions presented by Carpenter (2001). For objects with Megeath et al. (2012) ID numbers 612 and 792, the A_V calculated in this manner leads to slightly negative values that are nonphysical, and thus here we adopt A_V values of 0.0 (Table 2). Figure 3 shows the $J-H$ vs. $H-K_S$ color-color diagram for the sample with the CTTS locus shown as a solid red line. The dwarf branch from Bessell & Brett (1988) and the CTTS locus shown in Figure 3 have been converted to the 2MASS photometric system as described above. The distribution of the visual extinction values gathered from the literature and

calculated in this work from the CTTS locus for the sample is shown in Figure 4. The A_V distribution indicates that the literature values tend to be lower than those calculated from the CTTS locus, likely because the literature values (taken mostly from Fang et al. 2009, 2013 and Kim et al. 2016) were calculated using photospheric colors based on available spectral types, which biases the distribution towards low extinction values where spectral typing is more accurate.

The values for L and \dot{M} are collected from the literature (Fang et al. 2009, 2013; Kim et al. 2013, 2016). Fang et al. (2009, 2013) use the $H\alpha$, $H\beta$, and HeI line luminosities, as well as the full width of $H\alpha$ at 10% to derive \dot{M} . Accretion rates from Fang et al. (2009) and Fang et al. (2013) agree within 50–250%. Kim et al. (2013, 2016) use the $\text{Pa}\gamma$, $\text{Pa}\beta$, and $\text{Br}\gamma$ line luminosities. Accretion rates from Kim et al. (2016) range from being $\sim 3\%$ to $\sim 7,000\%$ of the values in Fang et al. (2013) for the same object. These differences in mass accretion rates could be due to variability and/or differences in observational proxies (i.e., the lines used to calculate the mass accretion rates). We adopt the most recently published values.

We note that using Infrared Telescope Facility/Spex (Rayner et al. 2003) observations Kim et al. (2016) determined objects with Megeath et al. (2012) ID numbers 250 and 980 to be binaries. Kounkel et al. (2016), using the *Hubble Space Telescope* and the NICMOS and WFC3 cameras, searched for binaries with separations between 100 and 1,000 AU; 25 out of 169 of the objects in our Class II sample are included in this survey. Of these 25, eight are found to be binaries; these are objects 315, 369, 421, 523, 526, 561, 579, and 950. Of the known binaries, only two (561 and 579) remain in the sample after object flagging. With roughly 15% of the sample studied for binaries (and mostly at large separations), we cannot rule out that other objects in our sample are binaries.

3.2. Spectral Energy Distributions

We constructed the SEDs of the sources using data from 2MASS at the J -, H -, and K_S - bands, *Spitzer* IRAC at bands 3.6, 4.5, 5.8, and 8 μm , and *Spitzer* MIPS at 24 μm , along with the *Herschel* PACS 70 μm photometry presented in this work. Additionally, 40 of the objects have V - and I -band photometry from Hsu et al. (2012)

and 64 have *Spitzer* Infrared Spectrograph (IRS; Houck et al. 2004) spectra from Kim et al. (2013, 2016) with an additional 18 available in the Combined Atlas of Sources with Spitzer IRS Spectra archive (Lebouteiller et al. 2011). In Figure 5, we present the SEDs of the 98 sources that have A_V determinations. In Figure 13, we show the SEDs of the 58 sources that have A_V determinations, but have been flagged as described in Section 3.1. Objects without A_V values lack 2MASS data, and thus we cannot calculate A_V from the CTTS locus. The values of A_V that are listed in Table 2 were used to correct the photometry, and spectroscopy if available, for extinction. Objects with $A_{K_s} < 0.3$ are dereddened using the Mathis (1990) extinction law with $R_V = 3.1$, and those with $A_{K_s} \geq 0.3$ are dereddened using the McClure (2009) extinction curves. Each object is listed with its corresponding identification number from Megeath et al. (2012); spectral type, if available; and A_V .

The dereddened SEDs are plotted with the photospheric fluxes corresponding to the adopted spectral type (Kenyon & Hartmann 1995), scaled at the J -band where the peak of the photospheric emission of K- and M-type stars occurs, although excesses from accretion, hot gas, and hot dust may still contribute at this wavelength (Fischer et al. 2011; McClure et al. 2013a). For objects with spectral types later than M6.0 (i.e., M7.0 or M7.5 objects), M6.0 photospheres are shown. For objects with spectral type K8.0, K7.0 photospheres are shown. This is due to the lack of M7.0 and K8.0 spectral types in Kenyon & Hartmann (1995). The SEDs are also plotted with the median dereddened SED of Taurus in the K5.0–M2.0 spectral type range (Furlan et al. 2006). We use the Taurus median as a proxy for a typical protoplanetary disk. The Taurus median is scaled at the H -band, where the flux is still dominated by stellar emission in T Tauri stars. Here we have extended the median out to the $70 \mu\text{m}$ PACS wavelength using data from the *Herschel* Open Time Key Project’s Gas in Protoplanetary Systems, presented in Howard et al. (2013). Additionally, we plot the Taurus quartiles (i.e., the range within which 50% of the objects fall) for reference.

3.3. Disk Classification

To characterize the properties of the disks in our sample, we first determine if our objects are full disks (FDs) or transitional disks (TDs). FDs have optically thick material extending from the dust sublimation radius near the star to the outer disk. TDs contain holes or gaps in their dust distribution that can be inferred from a dip in the NIR and MIR flux in the SED (see Espaillat et al. 2014 for a review).

A considerable number of ways to identify TDs are outlined in the literature. These include the use of photometric colors and spectral indices, essentially slopes between photometry or spectral points (e.g., Furlan et al. 2006, 2009, 2011; Gutermuth et al. 2008; Fang et al. 2009, 2013; Cieza et al. 2010; Merín et al. 2010; Muzerolle et al. 2010; Kim et al. 2013, 2016; Koenig et al. 2012; Ribas et al. 2013). The photometric bands for the colors and indices should be chosen such that they effectively separate the TDs from the FD population, while minimizing biases from emission features, such as silicate features. We implement some of the color and index criteria used in the literature on our sample; we did not use classification systems that relied on IRS spectra since we do not have these data for our entire sample. Here we list the criteria implemented on our sample,

1. Fang et al. (2009, 2013) use K_S -[5.8] vs. [8]-[24] with boundaries for TDs defined by $[8]-[24] \geq 2.5$ and K_S -[5.8] $\leq 0.56 + ([8]-[24]) \times 0.15$.
2. Merín et al. (2010) use [3.6]-[8] vs. [8]-[24] with two regions separating systems with only photospheric fluxes and systems with some excess flux above the photosphere in the IRAC bands: Region A: $0.0 < [3.6]-[8] < 1.1$ and $3.2 < [8]-[24] < 5.3$; Region B: $1.1 < [3.6]-[8] < 1.8$ and $3.2 < [8]-[24] < 5.3$. Kim et al. (2013), using their Orion A sample, finds that Region A corresponds to classical TDs, defined as disks with Inner Disk Excess Fractions (IDEF) < 0.25 (see Equation 8 of Kim et al. 2013) and Region B to weak-excess TDs, $0.25 \leq \text{IDEF} < 0.5$, and pre-transitional disks, $\text{IDEF} \geq 0.5$.
3. Cieza et al. (2010) use $[3.6]-[24] > 1.5$ and $[3.6]-[4.5] < 0.25$ as the broad criteria for

TDs in their Ophiuchus sample.

4. Muzerolle et al. (2010) use slopes $\alpha_{[3.6]-[5.8]} < -1.8$ and $-1.5 \leq \alpha_{[8]-[24]} \leq 0.0$ for weak excess sources (sources with some MIR excess that is above the photosphere but below what we would expect for optically thick material; see Muzerolle et al. 2010 for full discussion) and $\alpha_{[8]-[24]} > 0.0$ for classical TDs.

The criteria discussed here are shown in Figure 6. To classify disks as transitional in our sample, we require that they meet three out of the four criteria listed above (we consider objects to be candidate TDs if they meet one or two, but not three, of the criteria). We identify 24 objects in our sample as TDs and an additional 25 as candidates; the TDs and candidate TDs are listed in Table 3. This leads to $\sim 23\%$ TDs among the sample with available A_V , eight of which are newly identified. The eight newly identified TDs have Megeath et al. (2012) ID numbers of 227, 250, 278, 387, 403, 619, 689, and 811. A TD fraction of $\sim 23\%$ is higher than the $\sim 10\%$ at 1.5 Myr inferred by Muzerolle et al. (2010) using *Spitzer* photometry. The discrepancy could be due to broader selection criteria than Muzerolle et al. (2010), a bias that the TDs tend to be bright at PACS 70 μm because of illuminated edge of the disk (discussed more in Section 4.2), or to uncertainties in the age of L1641. We note that a TD identification criterion using Wide-field Infrared Survey Explorer (WISE; Wright et al. 2010) 12 μm photometry and *Herschel* PACS 70 μm photometry has been used by Ribas et al. (2013), Bustamante et al. (2015), and Rebolledo et al. (2015). These groups used the spectral index $\alpha_{[12]-[70]} > 0.0$ to identify TDs. A similar method can be used for this sample, using the IRAC 8 μm data instead of the WISE photometry. Using $\alpha_{[8]-[70]} > 0.0$ as an identifier for this sample leads to 21 TDs. Compared to the identifications reported in this work, 16 overlap with the TD sample of 24 (67% overlap), 3 with the candidate TDs, and 2 with the full disks.

3.4. L1641 Median SED

We present the median SEDs for the entire L1641 sample (Table 4), as well as the FD median (Table 5) and TD median (Table 6), along with their quartiles. In Figure 7 we show the median

of the FD and TD samples in L1641 compared to the Taurus median. We use photometry from the V -band to 70 μm to construct the median. We determine the dereddened fluxes using the A_V values listed in Table 2, as described in Section 3.2. In order to reduce spread in the SEDs due to differences in stellar parameters and unknown distances, we normalize each object’s SED to the median H -band flux for the sample, as is done for the Taurus median computed by Furlan et al. (2006), before computing the median at each photometry point. Flagged objects are not included in the median SED.

The median SED for the whole sample (FDs and TDs) is dominated by the FD flux as they are more numerous. The L1641 FD median follows the Taurus median quite well. When the TDs are separated from the FDs, a clear distinction arises between the two, namely, that the TD median is much lower than the FD median at NIR and MIR wavelengths, while it is slightly higher at 70 μm . A similar result was found for TDs with *Herschel* data in Chamaeleon by Ribas et al. (2013).

4. Comparison with Models

4.1. Description of Models

We use the D’Alessio irradiated accretion disk (DIAD) models (D’Alessio et al. 1998, 1999, 2001, 2006) to study to our protoplanetary disk sample, allowing us to identify trends in disk properties. These models calculate the structure and emission of accretion disks irradiated by the central star. The models include the effects of dust settling, by having two grain populations, each with a size distribution $n(a) \propto a^{-3.5}$ between a_{min} and a_{max} . The population in the upper layers has $a_{\text{max}} = 0.25 \mu\text{m}$, while the disk midplane population has $a_{\text{max}} = 1 \text{ mm}$ (D’Alessio et al. 2006). For both populations, $a_{\text{min}} = 0.005 \mu\text{m}$. We assume a dust mixture of silicates and graphite with silicate mass abundances relative to gas of 0.004 and graphite fractional abundances of 0.0025, with opacities calculated with Mie theory using optical constants from Dorschner et al. (1995) for olivine silicates and from Draine & Lee (1984) for graphite. The input model parameters that we keep fixed are the disk radius, the height of the directly irradiated inner disk edge or the “wall”, the viscosity parameter (α) which is parameter-

ized using the methods of Shakura & Sunyaev (1973), and the stellar parameters for the central star (mass, radius, and effective temperature). We vary the following input parameters: the mass accretion rate (\dot{M}), the inclination angle of the disk to the line of sight (i), and the dust-to-gas mass ratio in the upper layers of the disk in units of the total dust-to-gas mass ratio (ϵ , with a value of 1 corresponding to an unsettled disk, while a low value of 0.0001 corresponds to a factor 10^4 depletion of small grains in the upper layers of the disk atmosphere). We discuss the input values in Section 4.2.

4.2. Index Comparisons with Models

We calculate theoretical SEDs from our grid of models, convolving the theoretical fluxes with the filter response at each band to create synthetic colors which we use to calculate the indices for each model. We select the $n_{K_S-[70]}$ index (see Equation 1) as an indicator of the total flux in the PACS 70 μm band relative to the star. We adopted K_S -band magnitudes as our anchoring point instead of a shorter wavelength filter because the K_S -band is less affected by reddening and a large fraction of our sample is heavily reddened (Fig. 4). We performed a two-sample Kolmogorov-Smirnov (K-S) test between the $n_{K_S-[70]}$ and $n_{J-[70]}$ distributions for the total samples, the FDs, and the TDs separately and find that there is no significant difference between using J and K_S as our anchoring point.

In this work, we focus on the effects of varying mass accretion rates, inclinations, and dust settling and how these parameters affect our index comparison with observations in L1641. The mass of the disk depends on the surface density and radius. The surface density depends on \dot{M}/α . Here, when we fix α and the radius and vary \dot{M} , we are essentially varying the mass of the disk (D’Alessio et al. 1998).

Inclination can have significant effects on model SEDs (D’Alessio et al. 2006), especially in the edge-on case. When the disk is edge-on, the star is extinguished by the disk. We note that we do not expect any of the disks in this sample to be edge-on, since the extinction of the central star in the optical and near-infrared wavelengths would have prevented these disks from being identified as Class II objects. Besides the edge-on case, the

closer to edge-on the disk is, the more of the hot inner wall that will be observed, making the NIR flux higher than a disk that is closer to face-on. The DIAD models assume a completely vertical inner wall at the dust sublimation radius for FDs; in the future, changes may be made to include curved walls (McClure et al. 2013b).

Dust settling is a marker of disk evolution. As small dust grains settle from the upper layers of the disk atmosphere to the disk midplane, the flux from MIR to FIR wavelengths decreases (D’Alessio et al. 2006). The NIR is dominated by the wall, which is unaffected by disk settling. Thus, NIR fluxes anchor our indices such that we can probe the degree of dust settling with the FIR.

We adopt the median spectral type of the sample, M1, to describe the stellar properties that we use as input to the model. Although the sample contains a wide range of spectral types, the use of a spectral index anchored at a stellar-dominated wavelength mitigates the effects caused by the choice of one spectral type to represent the sample. We adopt an age of 1 Myr and a mass of $\sim 0.4 M_\odot$ and a radius of $\sim 2 R_\odot$ for our M1 star, consistent with the Siess et al. (2000) isochrones. We use a T_{eff} of ~ 3600 K based on stellar temperatures given in Kenyon & Hartmann (1995). We vary (1) the mass accretion rate as $\log_{10}(\dot{M})$ from -10 to $-7.5 M_\odot \text{ yr}^{-1}$, sampled in steps of 0.5, (2) the inclination of the disk parameterized by $\mu = \cos(i)$ from 0.1 to 0.9, in steps of 0.1, and at 0.99 (nearly edge-on at $\mu = 0.1$, $\sim 84^\circ$, and very nearly face-on at $\mu = 0.99$, $\sim 8^\circ$), and (3) the dust settling, $\log_{10}(\epsilon)$, from -4 to 0 , in steps of 1.0. This results in a grid of 300 models. We use a constant value of α set to 0.01 and an outer radius for the disk at 300 AU. In Figure 8, we show that the synthetic model index distribution covers the observed distribution.

We do not include forward modeling analysis of the TDs in this work. Depending on the size of the gap in the disk, the 70 μm flux could be dominated by the wall emission, as opposed to the disk emission. Figure 9 shows an example TD model with a wall temperature of 150 K and a gap size of ~ 13 AU showing that for only the most unsettled disks does the disk emission dominate over the wall emission at 70 μm . As we aim to derive information about the disk properties, we cannot use 70 μm fluxes unless the gap size is known. Fu-

ture work will be done to use the DIAD models to model the TDs in detail.

4.3. Forward Modeling

We use forward modeling to reproduce the observed FD L1641 $n_{K_S-[70]}$ distribution using the DIAD models. We carried out 100 realizations (above this, there is minimal change), and in each, we randomly sampled the cumulative distributions of the grid of $\log_{10}(\dot{M})$, $\cos(i)$, and $\log_{10}(\epsilon)$ and calculated the $n_{K_S-[70]}$ index for that combination of model parameters. We repeated this until we found the distributions of these parameters that reproduced the observed distribution of $n_{K_S-[70]}$. We adopted a uniform distribution for parameters μ (assuming that disks are randomly oriented) and ϵ , i.e., we sample uniformly from an even distribution. To determine a cumulative distribution for the mass accretion rate, we used the \dot{M} values from the literature for the sample, as listed in Table 2. We only have mass accretion rates for a subset of the sample and these are likely biased towards higher values because these are more easily measured. Therefore, we do not expect to reproduce the observed distribution. We restrict the analysis sample to have mass accretion rates between $10^{-7.5}$ and $10^{-10} M_{\odot} \text{ yr}^{-1}$. The highest mass accretion rates ($>10^{-7.5} M_{\odot} \text{ yr}^{-1}$) are largely associated with high visual extinction values and we remove these to avoid uncertain measurements. We also remove low mass accretion rates ($<10^{-10} M_{\odot} \text{ yr}^{-1}$) as these may have chromospheric contamination (Ingleby et al. 2011). The adopted distribution of mass accretion rates is shown in the second column of Figure 10. We note that we use the 63 FD objects that have $n_{K_S-[70]}$ values (i.e., are not missing K_S -band measurements or extinctions), have mass accretion rates between $10^{-7.5}$ and $10^{-10} M_{\odot} \text{ yr}^{-1}$, and have not been flagged (for contamination by close sources and/or nebulosity, high A_V , or colors not representative of CTTS objects), as discussed in Section 2.

The resulting mean of the distributions that reproduce the observed $n_{K_S-[70]}$ distribution are shown in Figure 10, where the error bars indicate the standard deviation between the results of each realization. The results in Figure 10 indicate that the observed \dot{M} distribution is biased towards high values and that we may be missing lower accretion

rate values for the sample, as expected. The distribution for μ is consistent with a uniform distribution, except at very high inclinations. This is to be expected, since it is difficult to identify edge-on disks. The ϵ distribution is relatively uniform except at the extreme unsettled and settled ends of the parameter space. We discuss this result and put it into context with other regions in Section 5.

We also performed this analysis on a Taurus sample in order to compare the two regions. The Taurus $n_{K_S-[70]}$ indices are calculated for 23 Class II objects with K_S -band magnitudes from Kenyon & Hartmann (1995) and PACS 70 μm fluxes from Howard et al. (2013). We only use objects that were not classified as transitional disks in Howard et al. (2013) and have A_V values in Kenyon & Hartmann (1995). The objects are dereddened in the same way as described for the L1641 sample in Section 3.2. We compare the FD $n_{K_S-[70]}$ distributions for the two samples in Figure 11, finding that L1641 peaks at a slightly higher index. Mass accretion rates for 51 systems in Taurus are taken from Hartmann et al. (1998) and White & Ghez (2001) to produce the cumulative distribution that is sampled to reproduce the distribution of $n_{K_S-[70]}$. The sample for which we have mass accretion rates for and for which we have $n_{K_S-[70]}$ overlaps partially. We restrict the objects in the Taurus sample to have $-10.0 \leq \log_{10}(\dot{M}) \leq -7.5$ as we did for L1641. We use the same model grid and parameter space for both L1641 and Taurus since the index distributions cover the same range. These results are shown in Figure 12 and are discussed in Section 5.

5. Discussion

Here we discuss the degree to which the dust is processed or settled in our L1641 sample and compare this sample to other regions to place it into a larger context. The L1641 FDs show a wide range of dust settling. We find a trend in the dust settling toward a depletion factor of 100–1,000 ($\log_{10}(\epsilon) \sim -2 - -3$; Figure 10). For disks with $\log_{10}(\epsilon) = -1$, the gas-to-dust ratio in the atmosphere of the disk is a factor of ten larger than the 100 : 1 usually assumed for the ISM, with larger grains having settled toward the midplane. The observed disk indices are consistent with models that have low values of ϵ and thus

may be settled.

Age spreads and uncertainties make it difficult to directly link age and dust settling for a given region; however, we can compare global trends for L1641 to those found for the Taurus, Chamaeleon I, and Ophiuchus star-forming regions. Ophiuchus is slightly younger than our sample at <1 Myr (Luhman & Rieke 1999), Taurus is similarly aged at $\sim 1 - 2$ Myr (Kenyon & Hartmann 1995; Hartmann et al. 2001; Luhman et al. 2010; Andrews et al. 2013), and Chamaeleon I is slightly older with a median age of 2 Myr (Luhman 2004), although all regions have some age spread. Furlan et al. (2006, 2009), also using the DIAD models, find that Taurus, Ophiuchus, and Chamaeleon I all have dust depletion factors of 100 to 1,000 ($\log_{10}(\epsilon) \sim -2$ to -3), indicating that dust evolution and settling are well underway by even the first ~ 1 Myr. Similar conclusions were reached by Lewis & Lada (2016), who found that the median SEDs from $2-8 \mu\text{m}$ of all Class II objects in Orion A from Megeath et al. (2012), are consistent with a flat disk, indicative that a significant number of these disks has undergone a high degree of dust settling.

We performed a two-sample K-S test on the FD $n_{K_S-[70]}$ distributions for the L1641 and the Taurus samples and found that these distributions are statistically different (p-value ~ 0.02). The higher index values of L1641 could be caused by slightly less disk settling compared to Taurus or additional contamination from molecular cloud structures, or a combination of the two. The contamination may come from remnant material associated with the star or structures in the line of sight. We performed our statistical analysis on the Taurus sample described in Section 4.3 (Figure 12). The mean of the realizations shows that the Taurus FD $n_{K_S-[70]}$ distribution is only reproduced by a non-zero degree of dust settling. The Taurus $\log_{10}(\epsilon)$ distribution peaks at ~ -3 , corresponding to a dust depletion factor of $\sim 1,000$. The distribution trends toward lower ϵ values than L1641, indicating that Taurus is slightly more evolved than the similarly aged L1641. However, both distributions indicate that these young regions already show advanced degrees of dust processing and settling.

Theoretical predictions show that small dust grains (with large surface-to-mass ratios) will experience a strong drag force as they move through

the gas, causing them to settle to the midplane in a few thousand years while large, compact grains can settle even faster (e.g., Dullemond & Dominik 2004). The process of settling is complicated by the fact that turbulence can cause a mixing of dust grains in disks, counteracting settling; however, turbulence is not effective high in the disk atmosphere where the gas density is sufficiently low (Dullemond & Dominik 2004). If the gas velocities in the upper layers are low, then dust settling can occur more efficiently (e.g., Ciesla 2007; Flaherty et al. 2015, 2017). Thus the dust depletion in the FDs of L1641 may be indicative of low turbulence in the upper disk atmosphere. Dust settling increases the dust density in the disk midplane, enhancing further dust growth, indicating that even the FDs in L1641 may be in the process of forming planets (e.g., Goldreich & Ward 1973; Takeuchi & Lin 2002; Dullemond & Dominik 2004; Testi et al. 2014).

6. Summary and Conclusions

We present *Herschel Space Observatory* 70 μm PACS observations of 104 Class II objects in the Lynds 1641 region of the Orion Molecular Cloud A. We construct the SEDs of the 98 objects that have A_V determinations and perform a statistical analysis by comparing our results to the D’Alessio irradiated disk models (D’Alessio et al. 1998, 1999, 2001, 2006) to obtain global properties of the full disk sample. Additionally, we compare our Lynds 1641 sample directly to a sample in the Taurus star-forming region. From this analysis, we reach the following conclusions:

1. We identify 24 TDs ($\sim 23\%$) in our sample, including eight newly classified objects. There are 74 FDs in the sample.
2. We calculate the median SED for L1641 from V -band to $70 \mu\text{m}$. The FD median follows the scaled Taurus median well, while the TD median shows a much lower flux in the NIR and MIR and a slightly higher $70 \mu\text{m}$ flux than the scaled Taurus median.
3. We use forward modeling in conjunction with the D’Alessio models to find model parameter values that reproduce the observed FD $n_{K_S-[70]}$ distribution in L1641 and Taurus. This analysis indicates that Taurus is

slightly more evolved than our L1641 sample, which is already showing signs of dust processing with dust depletion factors of ~ 100 – $1,000$.

This work provides a large population of YSOs with FIR *Herschel* observations in a single star-forming region at a common distance. The *Herschel* data presented here offer further insight into this region, and more work can be done to study trends as a function of environment, evolutionary state, stellar mass and disk mass, and more. (Sub-)millimeter data will provide additional information that can be used with more detailed modeling to study these systems in further detail.

We thank the referee for comments that improved the paper. SLG, CCE, and AR acknowledge support from the National Science Foundation under CAREER Grant Number AST-1455042 and the Sloan Foundation. STM and WJF were supported by NASA through awards issued by JPL/Caltech. AMS acknowledges funding from Fondecyt regular (project code 1180350), the “Concurso Proyectos Internacionales de Investigación, Convocatoria 2015 (project code PII20150171), and the BASAL Centro de Astrofísica y Tecnologías Afines (CATA) PFB-06/2007. This work is based on observations made with the *Herschel Space Observatory*, a European Space Agency Cornerstone Mission with significant participation by NASA. The *Herschel* spacecraft was designed, built, tested, and launched under a contract to ESA managed by the *Herschel/Planck* Project team by an industrial consortium under the overall responsibility of the prime contractor Thales Alenia Space (Cannes), and including Astrium (Friedrichshafen) responsible for the payload module and for system testing at spacecraft level, Thales Alenia Space (Turin) responsible for the service module, and Astrium (Toulouse) responsible for the telescope, with in excess of a hundred subcontractors. PACS has been developed by a consortium of institutes led by MPE (Germany) and including UVIE (Austria); KU Leuven, CSL, IMEC (Belgium); CEA, LAM (France); MPIA (Germany); INAF-IFSI/OAA/OAP/OAT, LENS, SISSA (Italy); IAC (Spain). This development has been supported by the funding agencies BMVIT (Austria),

ESA-PRODEX (Belgium), CEA/CNES (France), DLR (Germany), ASI/INAF (Italy), and CI-CYT/MCYT (Spain). This work is also based [in part] on observations made with the *Spitzer Space Telescope*, which is operated by the Jet Propulsion Laboratory, California Institute of Technology under a contract with NASA. This publication makes use of data products from the Two Micron All Sky Survey, which is a joint project of the University of Massachusetts and the Infrared Processing and Analysis Center/California Institute of Technology, funded by the National Aeronautics and Space Administration and the National Science Foundation. This paper utilizes the D’Alessio et al. (1998, 1999, 2001, 2005, 2006) Irradiated Accretion Disk (DIAD) code. We wish to recognize the work of Paola D’Alessio, who passed away in 2013. Her legacy and pioneering work live on through her substantial contributions to the field.

A. Appendix

Here we present information about the protoplanetary systems that were flagged as described in Section 3.1. In Tables 7 and 8 we present the *Herschel* PACS fluxes and the stellar properties, respectively. For the flagged objects, we have spectral types for 31, luminosities for 40, A_V values for 59, and mass accretion rates for 24. Of the 59 A_V values, 40 are from the literature and the additional 19 are calculated in this work as described in Section 3.1. In Figure 13 we present the SEDs of the flagged systems. SEDs are computed as discussed in Section 3.2.

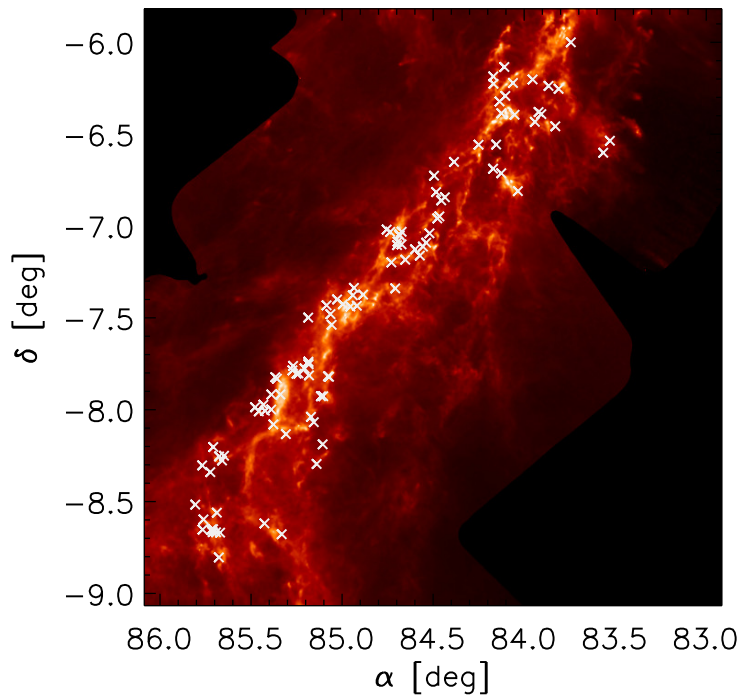


Fig. 1.—: L1641 column density, $N(\text{H})$, map shown on a log scale. The 104 objects in the sample analyzed here are marked with white \times -symbols. Figure adapted from Stutz & Kainulainen (2015); Stutz & Gould (2016).

TABLE 1
Herschel FLUXES

M12 Num	RA(J2000)	Dec(J2000)	F ₇₀ (Jy)
198	05:42:42.4	-08:48:13.8	0.403±0.020
217	05:41:19.6	-08:40:38.7	0.086±0.005
223	05:42:40.8	-08:40:08.6	0.041±0.003
225	05:42:46.1	-08:40:00.8	0.088±0.005
227	05:42:50.5	-08:39:57.5	0.265±0.014
228	05:42:52.5	-08:39:16.6	0.121±0.006
231	05:43:03.9	-08:39:09.2	0.063±0.004
232	05:42:50.0	-08:39:02.8	0.0247±0.0025
233	05:42:51.4	-08:39:01.9	0.042±0.003
250	05:41:42.4	-08:37:07.2	0.277±0.014
256	05:43:02.6	-08:35:48.8	0.089±0.005
263	05:42:45.0	-08:33:36.3	0.087±0.005
269	05:43:13.5	-08:31:00.5	0.189±0.010
278	05:42:53.6	-08:20:22.6	0.062±0.004
282	05:43:04.4	-08:18:10.8	0.069±0.004
284	05:40:33.7	-08:17:43.4	0.184±0.010
291	05:42:38.2	-08:16:35.4	0.161±0.008
294	05:42:42.1	-08:15:15.1	0.050±0.003
296	05:42:35.6	-08:15:01.8	0.059±0.004
307	05:42:49.8	-08:12:10.3	0.090±0.005
313	05:40:25.7	-08:11:16.8	0.0350±0.0025
342	05:41:14.0	-08:07:57.4	0.106±0.006
378	05:41:30.6	-08:04:47.9	0.85±0.04
383	05:40:37.3	-08:04:03.0	2.21±0.11
387	05:40:41.0	-08:02:18.6	0.067±0.004
399	05:41:49.7	-08:00:32.1	0.89±0.04
400	05:41:41.7	-08:00:18.4	0.083±0.004
402	05:41:33.4	-07:59:56.2	0.296±0.015
403	05:41:54.6	-07:59:12.4	0.053±0.004
411	05:41:43.7	-07:58:22.4	0.145±0.008
428	05:40:27.8	-07:55:36.3	0.115±0.006
429	05:40:24.9	-07:55:35.4	0.053±0.003
434	05:41:33.2	-07:55:02.1	0.107±0.006
435	05:41:21.4	-07:55:01.1	0.050±0.003
463	05:41:25.9	-07:49:50.6	0.202±0.010
466	05:41:28.0	-07:49:22.4	0.048±0.003
468	05:40:17.1	-07:49:14.4	0.280±0.014
471	05:40:18.5	-07:49:06.7	0.043±0.003
474	05:40:43.6	-07:48:47.8	0.063±0.004
476	05:40:59.9	-07:48:16.0	0.0179±0.0017
477	05:40:57.5	-07:48:08.8	0.236±0.012

TABLE 1—*Continued*

M12 Num	RA(J2000)	Dec(J2000)	F ₇₀ (Jy)
483	05:41:05.5	-07:47:07.6	0.219±0.011
485	05:40:49.3	-07:46:32.5	0.154±0.008
487	05:41:04.6	-07:45:40.1	0.231±0.012
488	05:40:44.1	-07:45:09.7	0.0379±0.0029
491	05:40:44.2	-07:44:43.5	0.060±0.004
494	05:40:44.4	-07:44:16.7	0.0337±0.0029
512	05:40:13.8	-07:32:16.1	1.03±0.05
525	05:40:44.7	-07:29:54.5	0.418±0.021
530	05:40:15.3	-07:28:46.8	0.227±0.012
546	05:39:49.1	-07:26:17.2	0.0153±0.0026
553	05:39:40.5	-07:26:03.5	0.021±0.003
556	05:40:20.4	-07:25:54.0	0.107±0.006
561	05:39:58.9	-07:25:33.5	0.65±0.03
574	05:40:06.5	-07:23:58.7	0.405±0.020
579	05:39:45.8	-07:22:37.2	0.0274±0.0022
582	05:39:32.3	-07:22:24.2	0.050±0.003
597	05:38:50.0	-07:20:18.5	0.62±0.03
598	05:39:44.3	-07:20:10.5	0.020±0.003
619	05:38:55.0	-07:11:53.7	0.069±0.004
626	05:38:36.6	-07:11:00.2	0.248±0.013
633	05:38:17.4	-07:09:39.5	0.349±0.018
637	05:38:23.9	-07:07:38.9	0.076±0.005
641	05:38:13.4	-07:06:43.4	0.061±0.004
644	05:38:47.7	-07:06:14.8	0.029±0.003
645	05:38:41.5	-07:05:59.3	0.156±0.008
653	05:38:09.1	-07:05:25.8	0.061±0.004
654	05:38:46.8	-07:05:09.1	0.059±0.004
663	05:38:44.0	-07:03:09.5	0.0201±0.0024
666	05:38:44.8	-07:02:47.0	0.0338±0.0027
673	05:38:04.8	-07:02:21.7	0.0322±0.0028
677	05:38:56.5	-07:01:55.4	0.057±0.004
680	05:38:41.5	-07:01:52.5	0.076±0.004
689	05:39:01.2	-07:01:09.5	0.047±0.003
729	05:37:54.5	-06:57:31.1	0.057±0.004
734	05:37:51.7	-06:56:51.8	0.062±0.004
751	05:37:49.3	-06:51:37.4	0.0347±0.0028
755	05:37:44.5	-06:50:36.8	0.112±0.006
761	05:37:56.0	-06:48:54.9	0.244±0.012
762	05:36:08.3	-06:48:36.3	0.311±0.016
792	05:37:58.8	-06:43:33.7	0.039±0.003
798	05:36:30.2	-06:42:46.3	0.032±0.004

TABLE 1—*Continued*

M12 Num	RA(J2000)	Dec(J2000)	F ₇₀ (Jy)
811	05:36:41.0	-06:41:17.8	0.097±0.006
818	05:37:32.4	-06:39:05.1	0.059±0.004
832	05:34:15.8	-06:36:04.5	0.64±0.03
847	05:37:00.1	-06:33:27.4	0.150±0.008
848	05:36:36.9	-06:33:24.2	0.106±0.007
853	05:34:06.9	-06:32:08.0	0.071±0.005
874	05:35:18.9	-06:27:25.3	0.109±0.007
887	05:35:45.9	-06:25:59.1	0.169±0.009
914	05:36:12.6	-06:23:39.4	0.155±0.008
920	05:35:37.3	-06:23:26.7	0.060±0.004
926	05:36:30.1	-06:23:10.1	0.251±0.013
930	05:35:41.0	-06:22:45.4	0.204±0.011
971	05:36:32.3	-06:19:19.9	0.210±0.011
980	05:36:24.8	-06:17:30.4	0.64±0.03
994	05:35:14.6	-06:15:12.5	0.186±0.010
1001	05:35:27.9	-06:14:15.0	0.0275±0.0029
1006	05:36:40.4	-06:13:33.3	0.078±0.005
1007	05:36:14.7	-06:13:16.9	0.071±0.004
1011	05:35:48.9	-06:12:07.7	0.171±0.009
1020	05:36:40.8	-06:11:08.2	0.106±0.007
1039	05:36:26.1	-06:08:03.7	0.230±0.012
1086	05:34:58.5	-06:00:00.5	0.162±0.009

NOTE.—For each object, we list the corresponding identification number from Megeath et al. (2012).

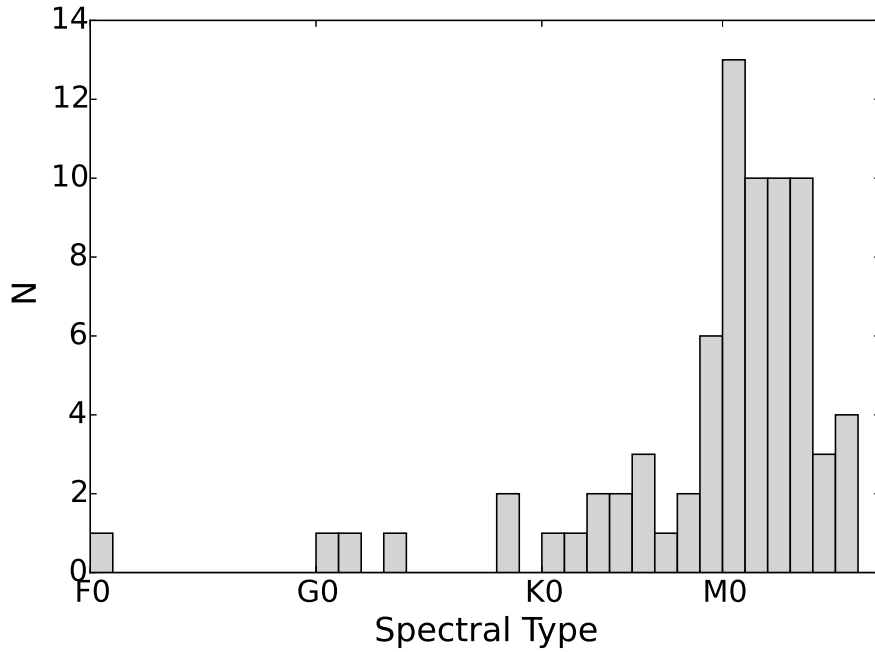


Fig. 2.—: Histogram of spectral types available in the literature for our L1641 sample. Bin size is one subclass. The median spectral type is M1.

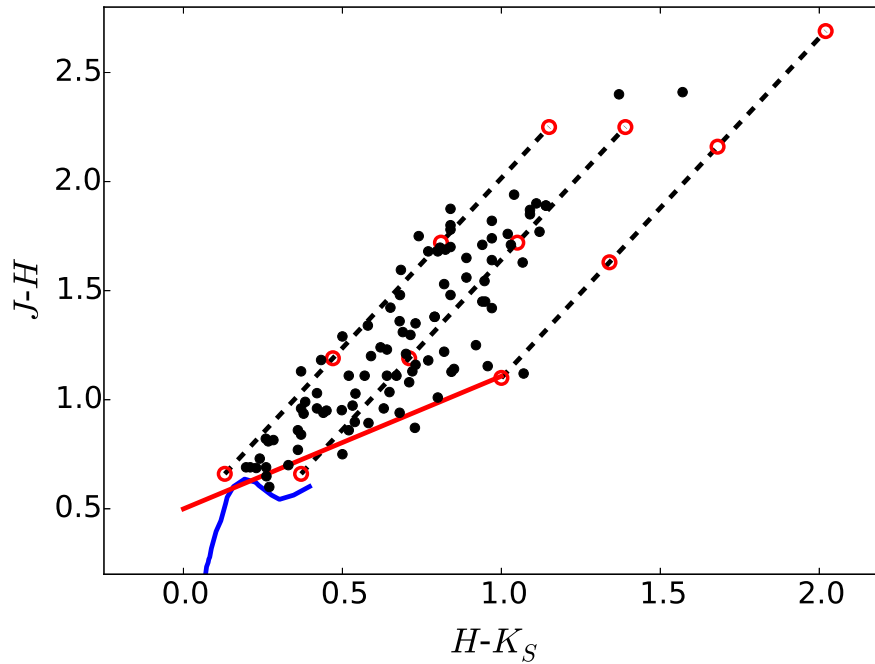


Fig. 3.—: $J-H$ vs. $H-K_S$ color-color diagram. The solid lines are the intrinsic colors of stars on the CTTS locus (red, Meyer et al. 1997) and dwarf branch (blue, Bessell & Brett 1988). The dashed lines are extinction vectors and the open red points show the extinction in increments of $A_V=5$.

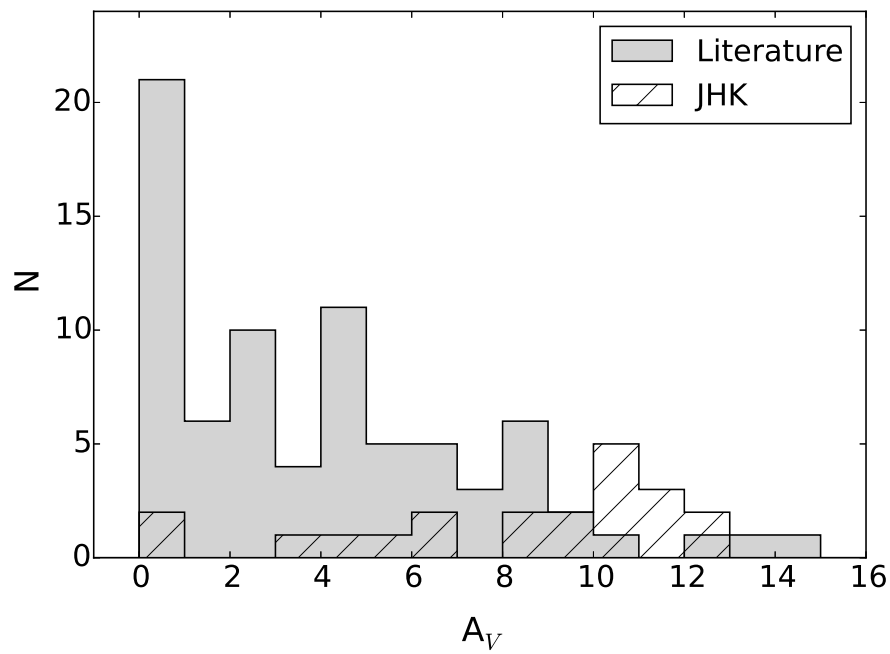


Fig. 4.—: Histogram of visual extinctions in our sample. Objects with values of A_V from the literature are shown in gray. The hatched region represents those objects whose A_V values were calculated in this work from the $J-H$ and $H-K_S$ colors and the CTTS locus.

TABLE 2
STELLAR PROPERTIES

M12 Num	SpT	SpT Ref.	A_V	A_V Ref.	L (L_\odot)	L Ref.	$\log \dot{M}$ ($M_\odot \text{ yr}^{-1}$)	\dot{M} Ref.
198	M2.0	a	7.71	b	2.17	b	< -8.29	b
217			10.82	CTTS J-H				
223	M2.5	a	0.91	b	0.25	b	-8.2	c
225	K4.0	a	5.46	b	4.04	b	< -8.5	c
227	K0.0	a	7.2	c	2.501	c		
228			6.21	CTTS J-H				
231	M1.5	a	4.7	b	0.95	b	-8.6	c
232			6.21	CTTS J-H				
233			6.72	b	3.54	b		
250	K1.0	a	5.43	b	11.71	b	-8.2	b
263	M2.5	a	5.3	c	0.527	c	< -9.4	c
269	M3.0	b	6.92	b	0.47	b	-8.02	b
278	K6.0	a	4	c	0.896	c	< -8.6	c
282	M2.5	a	2.92	b	0.35	b	-9.2	b
284			10.82	CTTS J-H				
291			8.25	CTTS J-H				
294	M3.0	a	3.4	b	0.32	b	-9.15	c
296	M2.0	a	2.14	b	0.35	b	-9.05	b
307	K7.0	a	4.1	c	0.575	c	-7.75	c
313	M3.0	a	5.3	CTTS J-H				
342	M2.0	a	1.41	b	0.95	b	< -8.52	b
378	K7.0	d	6.88	b	1.95	b	-6.74	d
383	F	d	6.6	b	59.31	b		
387	M0	d	7.9	d	1.126	d		
399	K5.0	d	0.03	b	5.83	b	-6.69	d
400	M0.0	a	4.5	d	0.047	d		
402	M1.5	d	8	b	1.05	b	< -9.09	b
403	K3.5	d	5.07	b	1.9	b	-8.4	d
411	M7.5	a	0.59	b	0.4	b	-8.22	b
428			8.46	b	1.05	b		
429	M3.0	a	8.2	d	1.723	d	-7.15	d
434	K7.0	a	0.9	b	0.55	b	-8.05	c
463	K7.0	a	4.26	b	1.03	b	< -8.96	b
466	M4.0	a	0	c	0.014	c	-10.7	c
468			8.55	CTTS J-H				
471			9.07	CTTS J-H				
476	M3.0	a	4.2	d	0.187	d	-8.92	d
477	M1.0	a	4.6	d	0.566	d	-8.26	d
483	G1.0	d	10.6	d	8.105	d	-6.54	d
485	M0.0	a	6.33	b	0.52	b	< -9.55	b
487	M0.5	a	2.1	c	1.134	c	< -9.15	c

TABLE 2—*Continued*

M12 Num	SpT	SpT Ref.	A_V	A_V Ref.	L (L_\odot)	L Ref.	$\log \dot{M}$ ($M_\odot \text{ yr}^{-1}$)	\dot{M} Ref.
488			10.77	CTTS J-H				
491			12.26	CTTS J-H				
494			9.85	b	0.36	b		
512	M5.5	a	4.1	CTTS J-H				
525	M1.0	a	4.26	b	1.13	b	-6.8	c
530			9.94	CTTS J-H				
556	M1.5	a	0.87	b	0.33	b	-8.67	b
561			13.1	b	2	b		
574	M3.0	a	5.7	c	0.509	c	-8.3	c
579			14.6	b	4.17	b		
582	K3.0	a	0.39	b	0.14	b	-9.92	b
597			3.38	CTTS J-H				
598			11.95	CTTS J-H				
619			12.54	CTTS J-H				
626	M4.0	a	4.2	c	0.8	c	-7.75	c
633	M3.0	a	4.2	b	1.07	b	< -8.47	b
637	K8.0	a	1.5	c	0.978	c	-8.8	c
641	K4.5	d	8.89	b	2	b		
644	M1.0	d	10.67	CTTS J-H				
653	K2.0	a	3.4	c	2.045	c	-8.4	c
654	M0.5	a	4.3	d	0.243	d	-8.94	d
663			11.26	CTTS J-H				
666			11.34	CTTS J-H				
673	M5.0	a	2.7	d	0.136	d		
677			10.7	CTTS J-H				
680	M2.0	a	2.6	d	0.183	d		
689	M3.0	a	3.5	c	0.339	c	-8.8	c
729	K7.0	a	0.9	d	0.939	d		
734	M2.4	a	1.4	d	1.324	d	-7.29	d
751	M3.5	a	1.41	b	0.31	b	-9.31	b
755	M1.0	a	0.66	b	0.45	b	-7.9	c
761	M0.0	b	8.25	b	1.04	b		
762	M2.5	a	2.31	b	0.85	b	-7.79	d
792			0.0	CTTS J-H				
798	M1.5	a	8.01	b	1.41	b	-8.09	d
811	M5.0	a	0.4	c	0.197	c	-9.85	c
818	M3.0	a	0	c	0.228	c	-10.1	c
832	G8.0	e	0.42	CTTS J-H				
847	G3.0	a	2.61	b	10.44	b	-7.89	b
848	K7.5	a	3.94	b	2.05	b	-6.35	b
853	M0.0	a	0.24	b	0.15	b	< -10.6	c

TABLE 2—*Continued*

M12 Num	SpT	SpT Ref.	A_V	A_V Ref.	L (L_\odot)	L Ref.	$\log \dot{M}$ ($M_\odot \text{ yr}^{-1}$)	\dot{M} Ref.
874	M4.0	a	0	d	0.187	d	-8.9	d
887	G0.5	c	9.8	c	13.259	c	-6.9	c
914	M5.0	a	0.4	d	0.232	d	-9.83	d
920	M2.5	a	0.21	b	0.3	b	< -8.82	b
926	K6.5	a	0.9	d	0.45	d		
930	M0.0	a	1	d	1.839	d	-7.93	d
971	G8.0	a	2.8	c	4.469	c	< -8.15	c
980			0.35	b	8.82	b	-7.85	b
994	M1.0	a	2.3	d	0.569	d	-8.92	d
1001	K8.0	a	2.6	c	0.723	c	-8.35	c
1006	M0.5	a	0.41	b	0.45	b	< -9.62	b
1007	M1.5	a	0.2	d	0.355	d	-8.18	d
1011	K4.0	a	0.9	c	1.736	c	-7.65	c
1020	K2.0	a	12.3	b	1.6	b		
1039	M0.0	a	1.78	b	1.5	b	< -8.77	b
1086	M0.0	a	0.08	b	0.66	b	-8.51	b

NOTE.—References: ^aHsu et al. (2012), ^bKim et al. (2016), ^cFang et al. (2013), ^dFang et al. (2009), ^eHsu et al. (2013). For sources with an A_V reference of CTTS J-H, visual extinctions were measured in this work as described in Section 3.1.

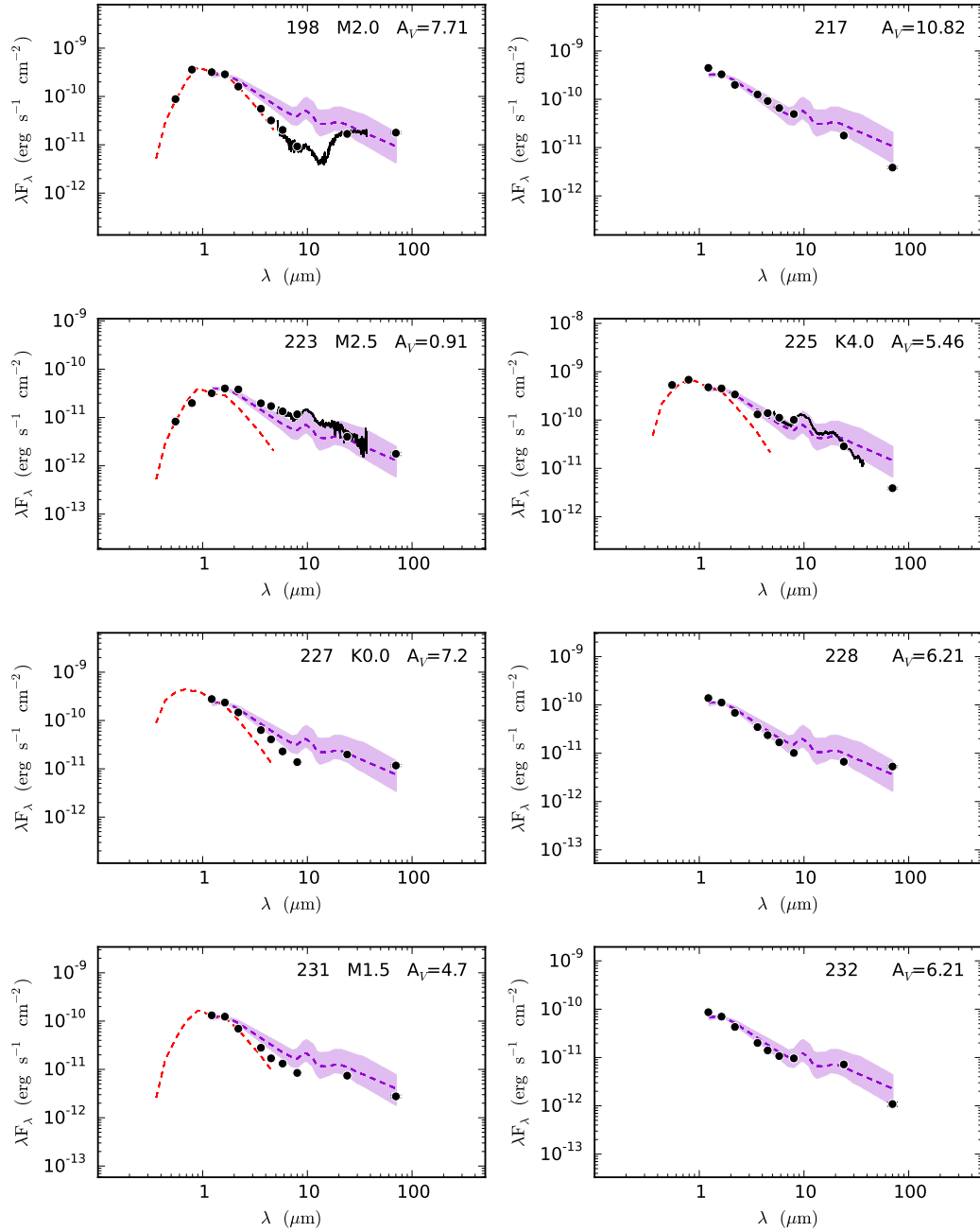


Fig. 5.—: SEDs for the non-flagged L1641 sample. Photometry and IRS spectra (where available) shown here are dereddened, as described in Section 3.2. Objects are identified by their Megeath et al. (2012) number, and we include the adopted spectral type and value of reddening, as given in Table 2. Photospheric fluxes for the adopted spectral type (red dashed lines) are from Kenyon & Hartmann (1995). The Taurus median, shown as the purple dashed lines, and the Taurus quartiles, shown as the shaded regions, are from Furlan et al. (2006) and data are from Howard et al. (2013).

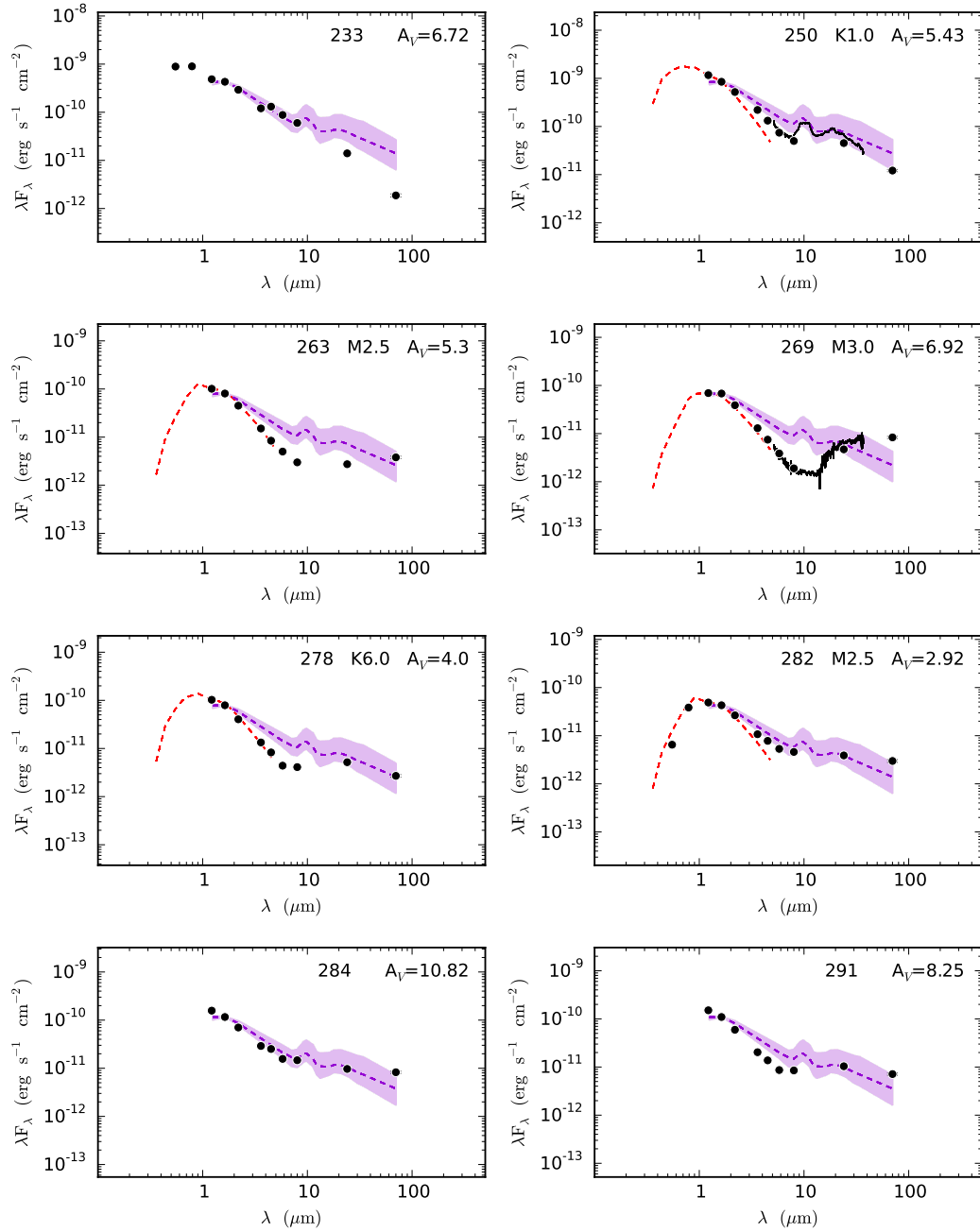


Fig. 5.— Continued

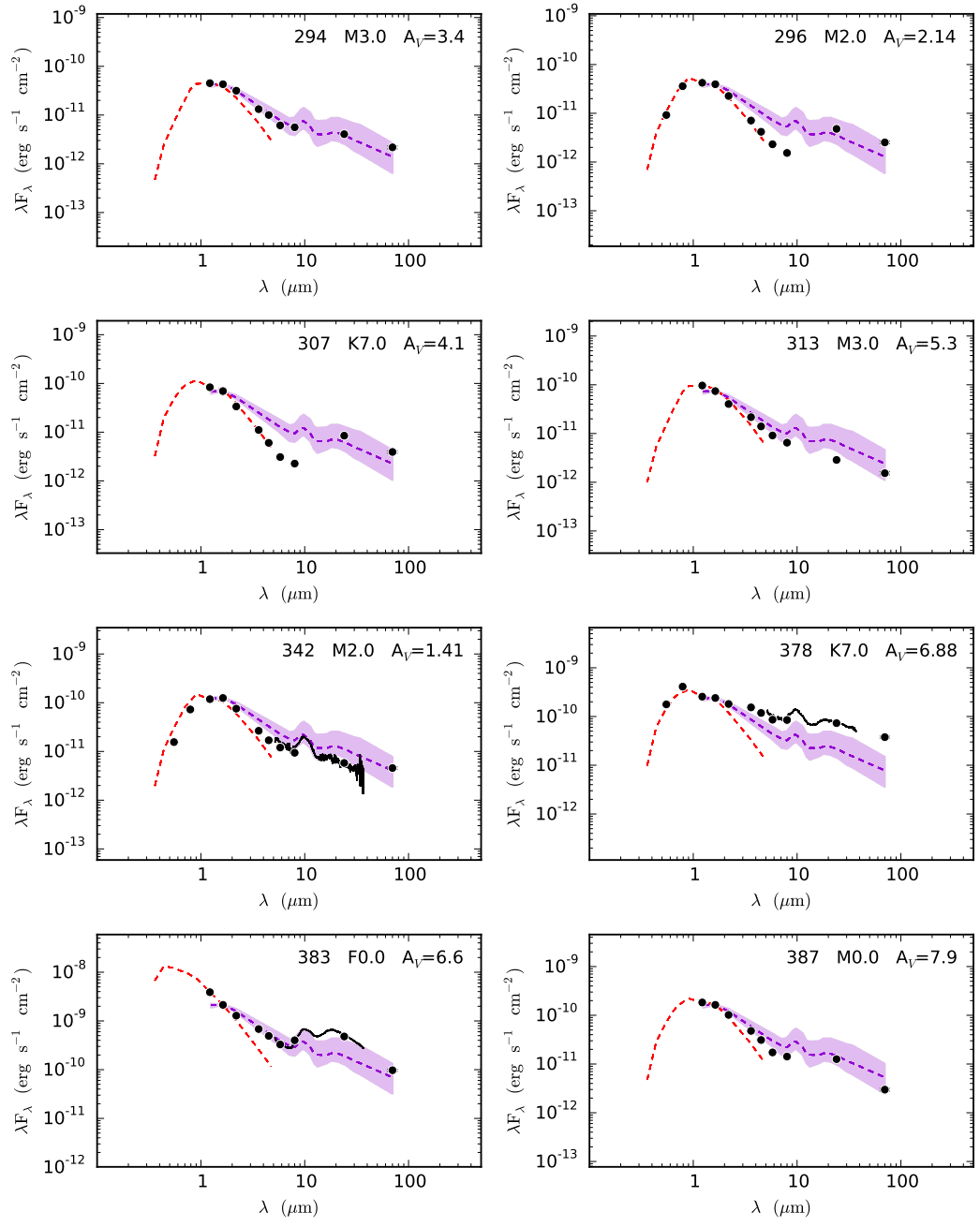


Fig. 5.— Continued

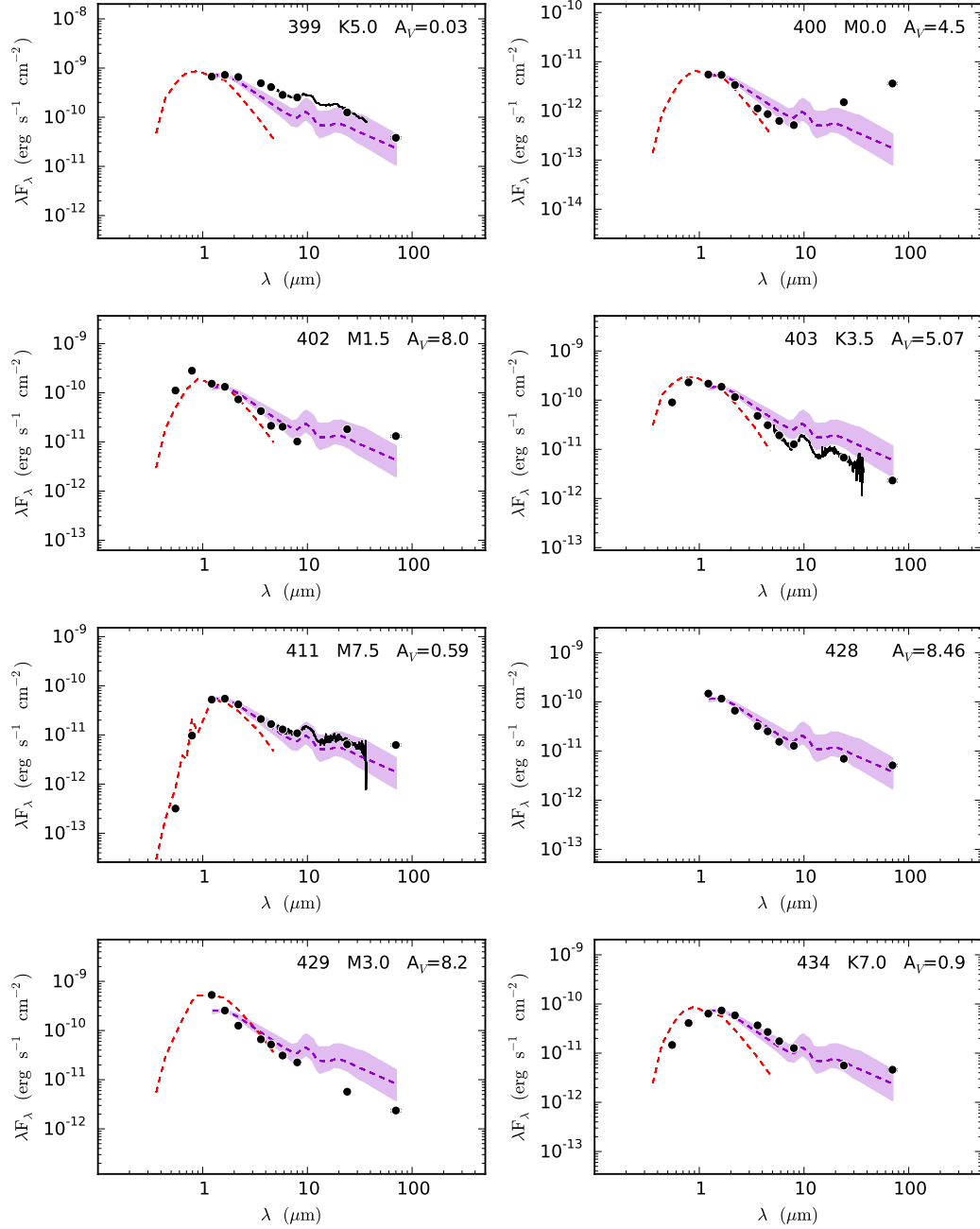


Fig. 5.— Continued

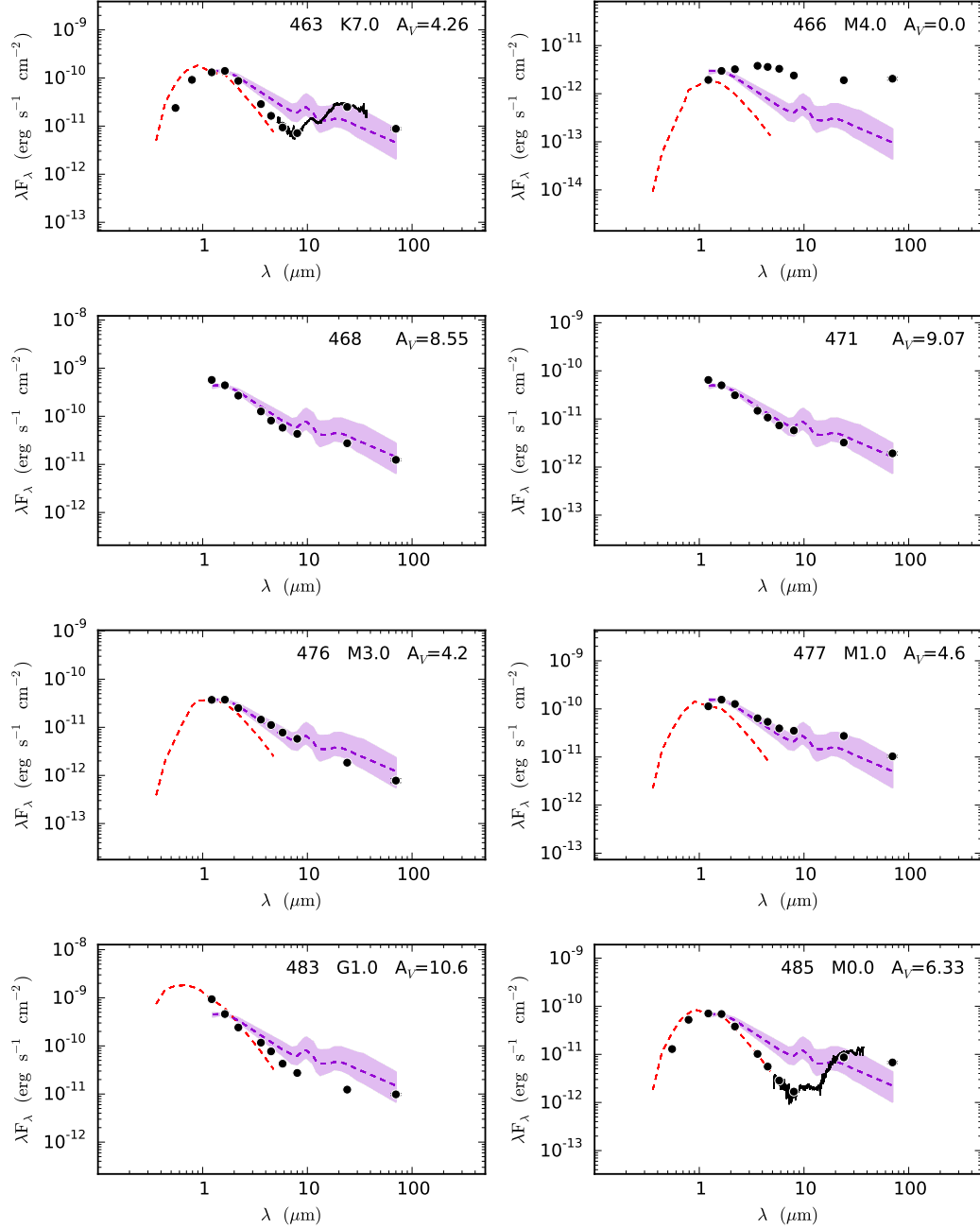


Fig. 5.— Continued

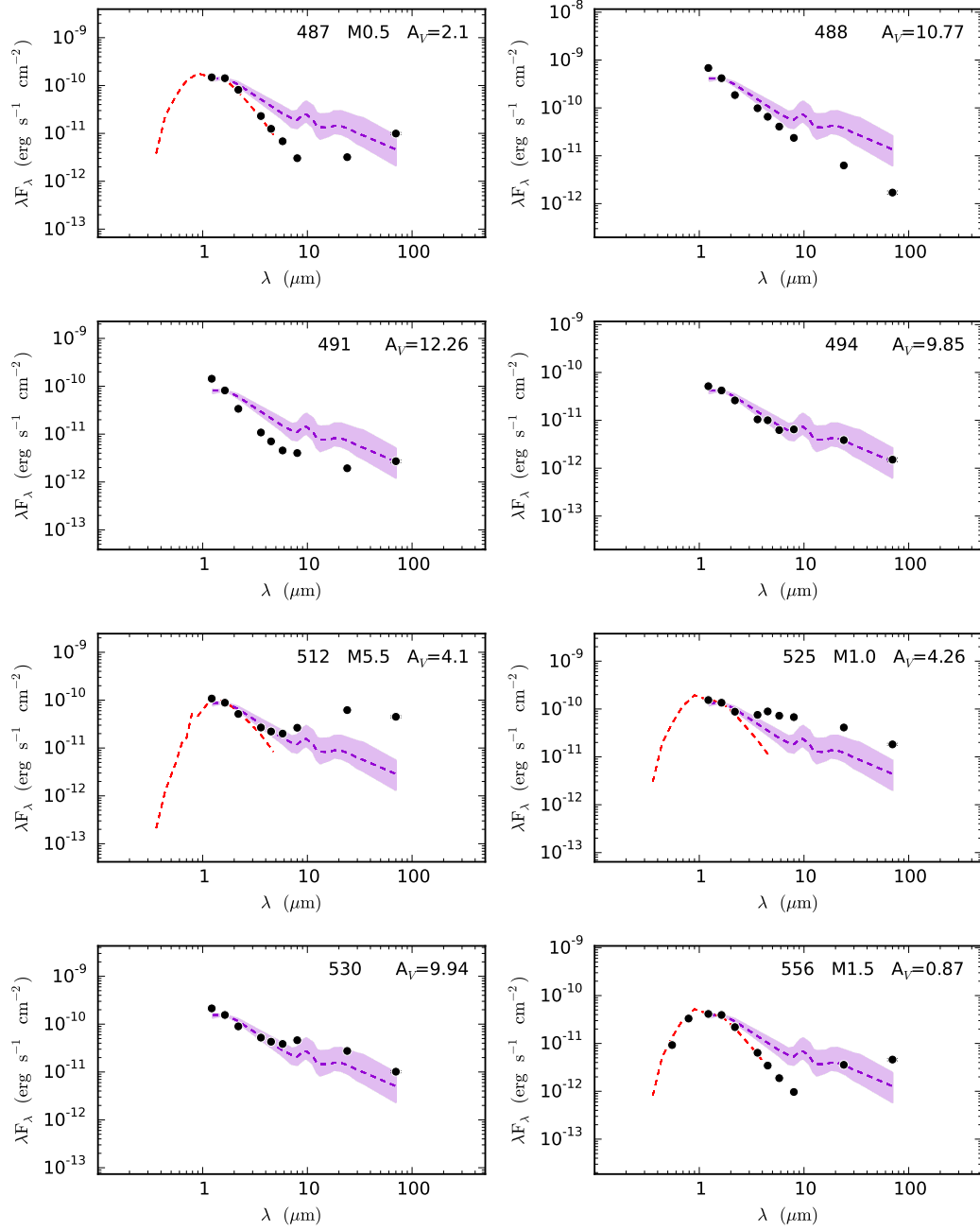


Fig. 5.— Continued

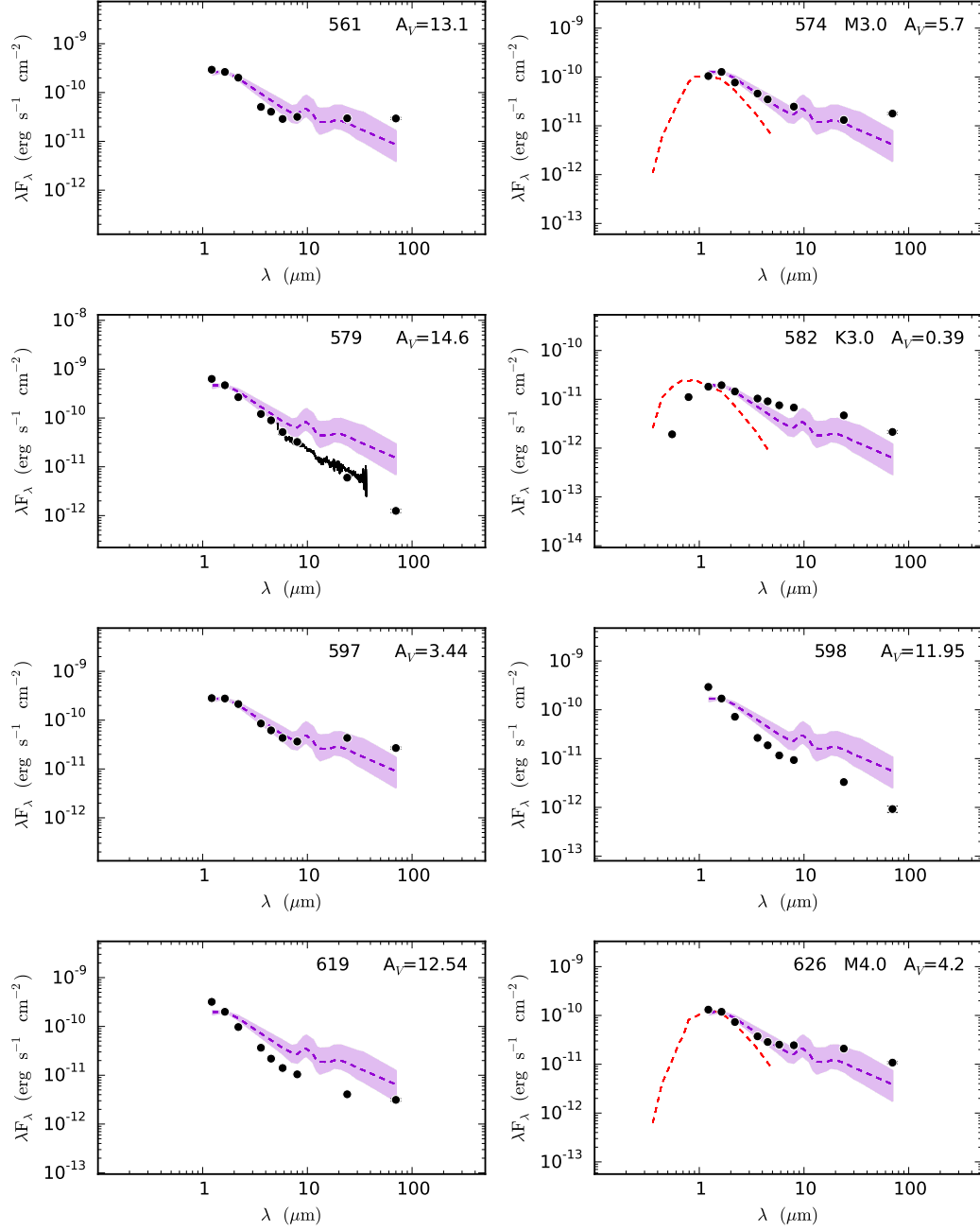


Fig. 5.— Continued

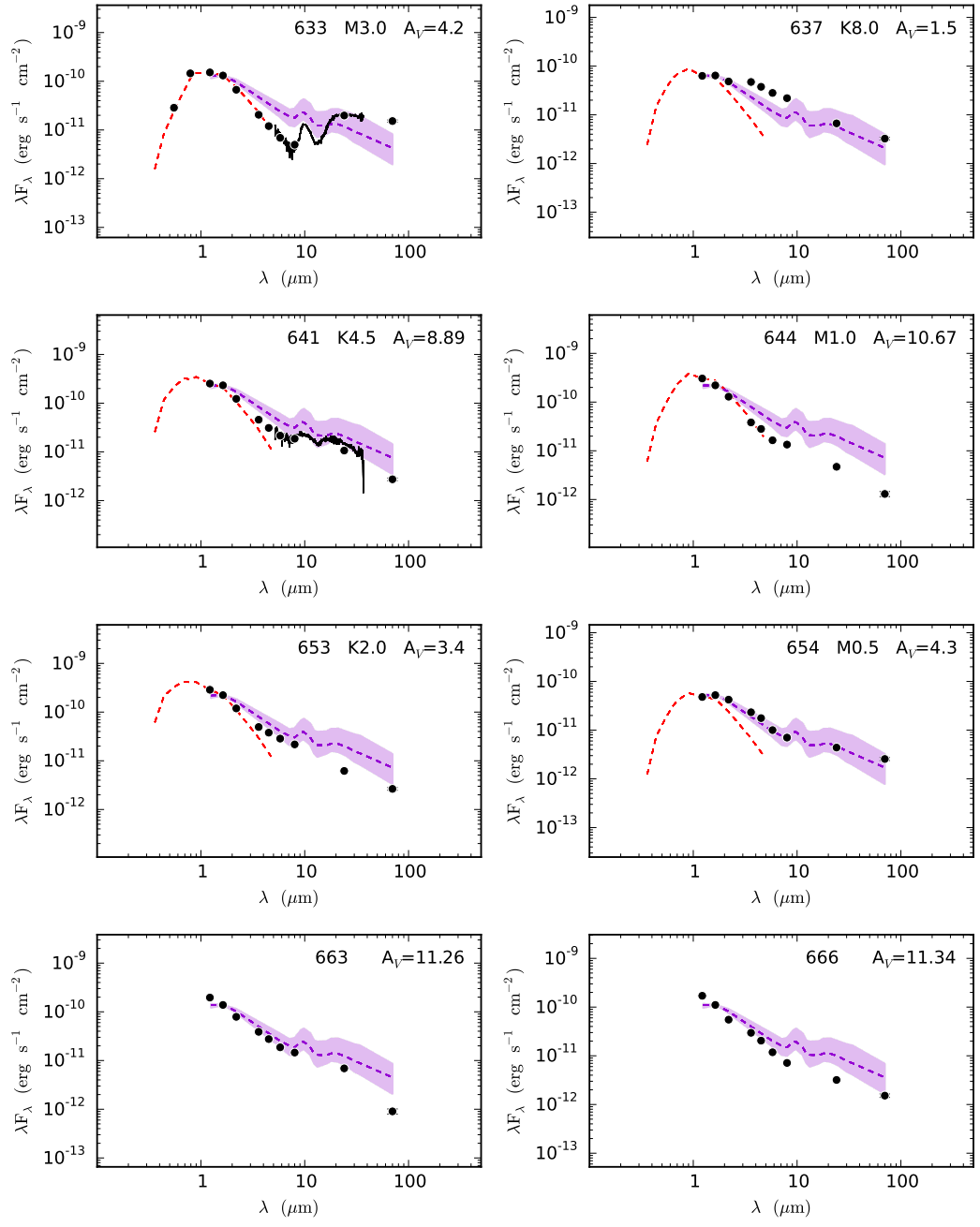


Fig. 5.— Continued

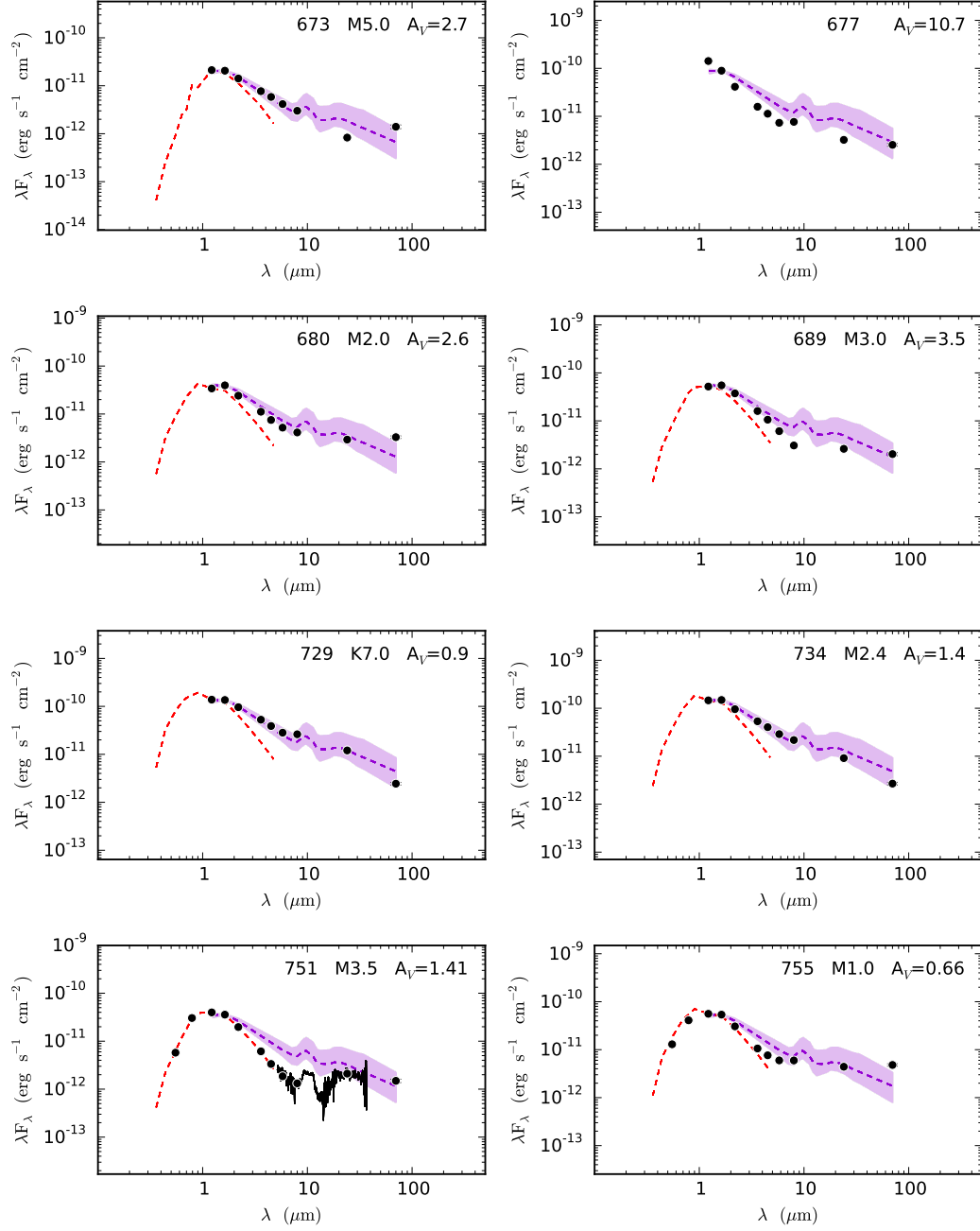


Fig. 5.— Continued

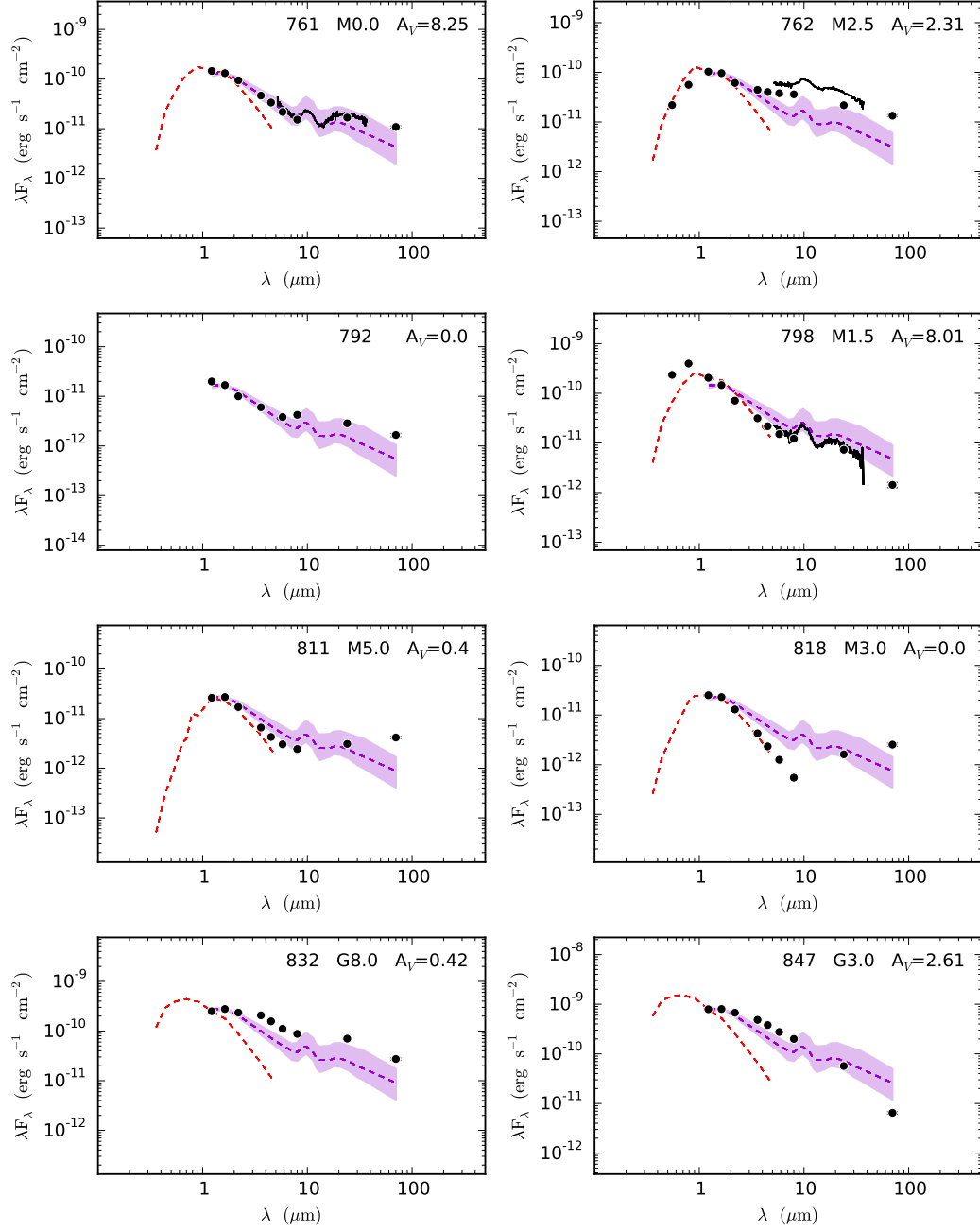


Fig. 5.— Continued

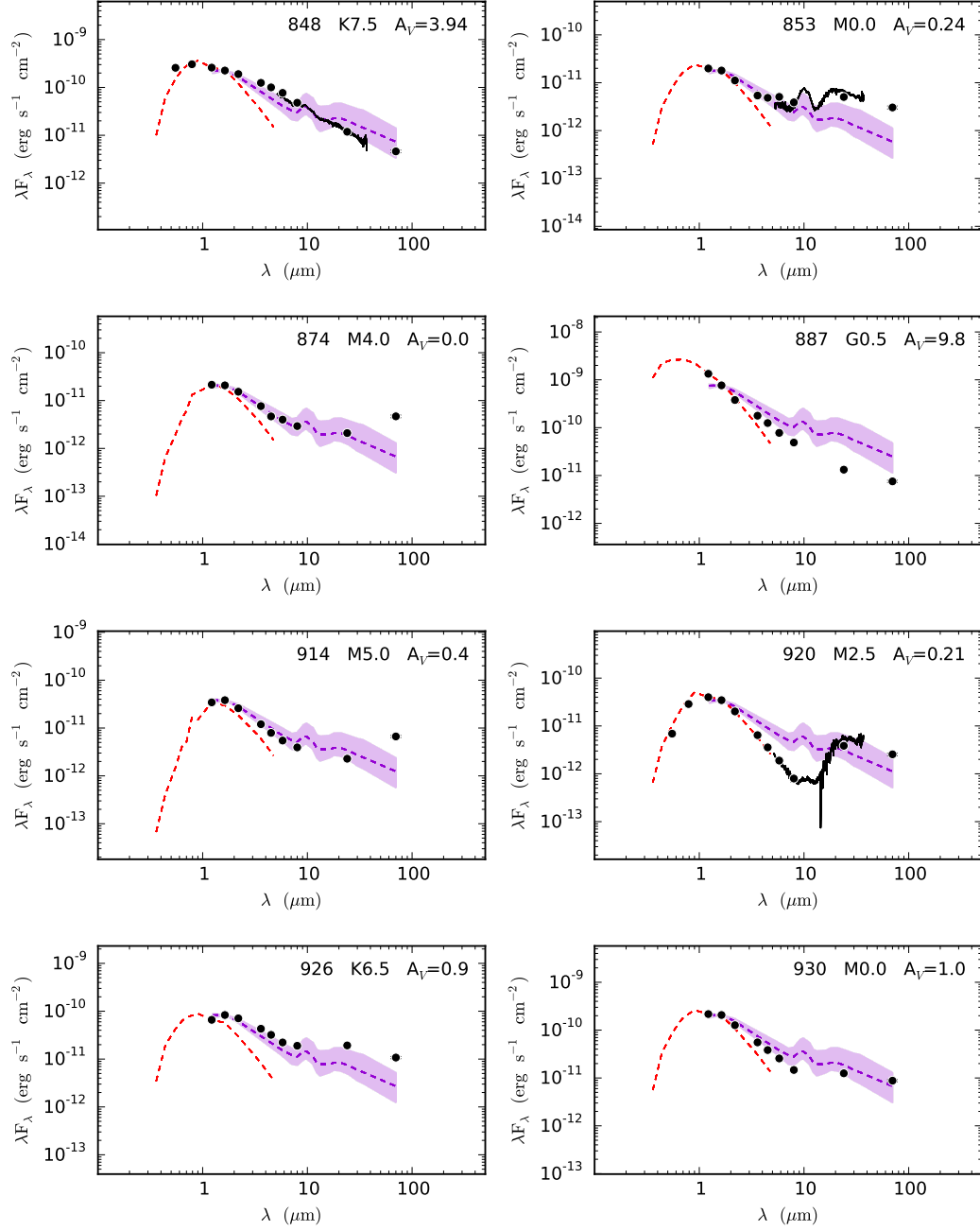


Fig. 5.— Continued

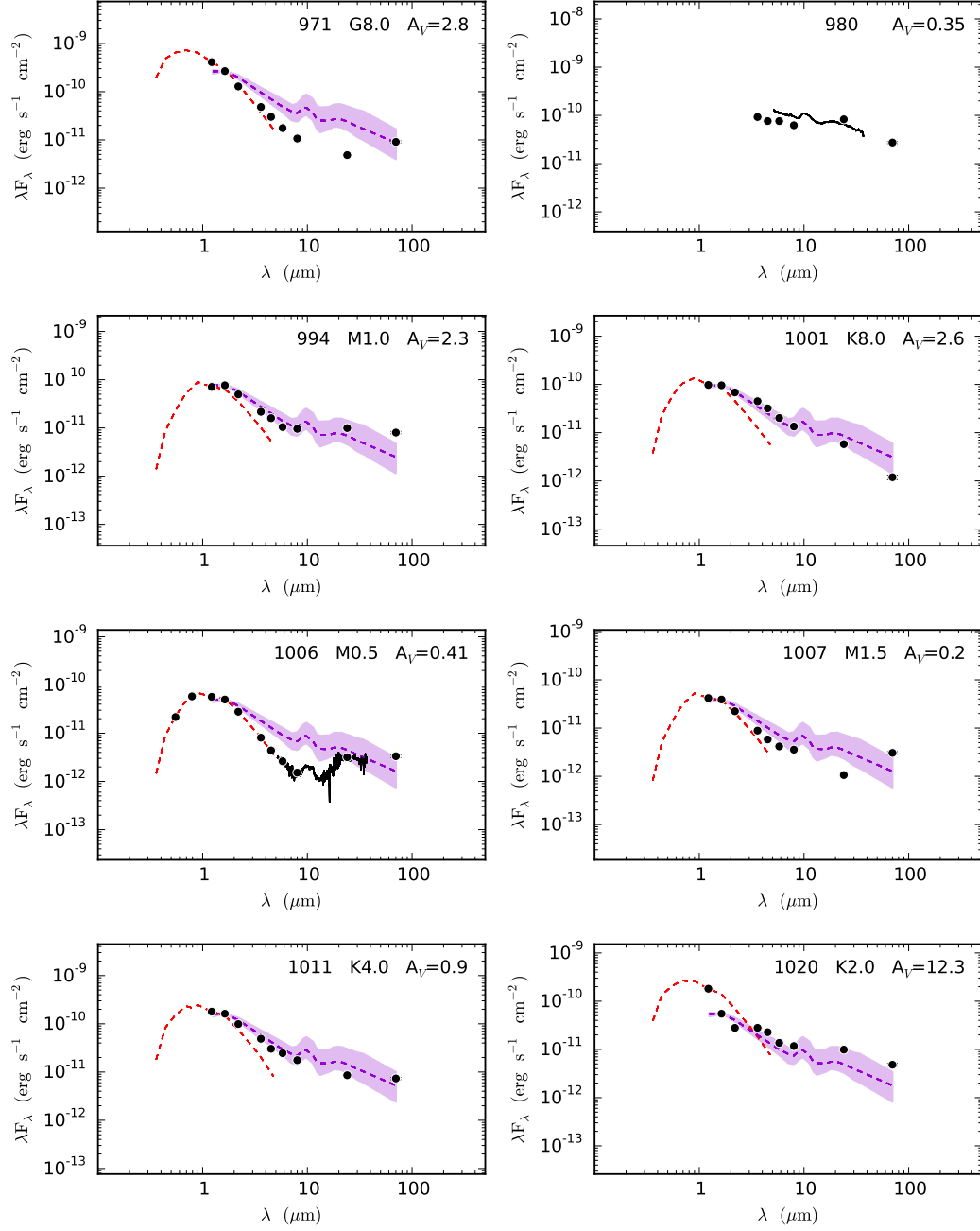


Fig. 5.— Continued

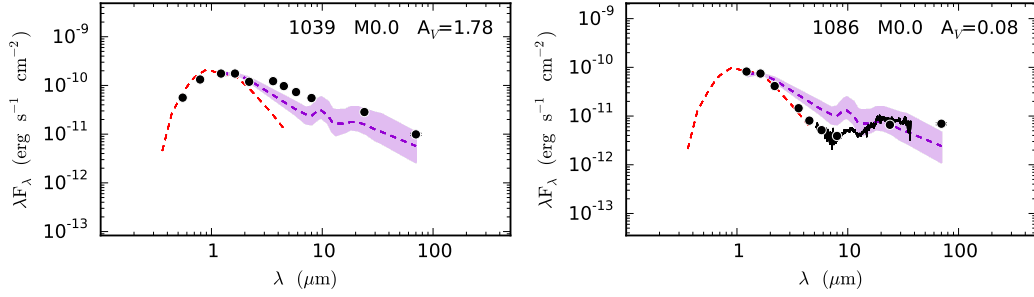


Fig. 5.—: Continued

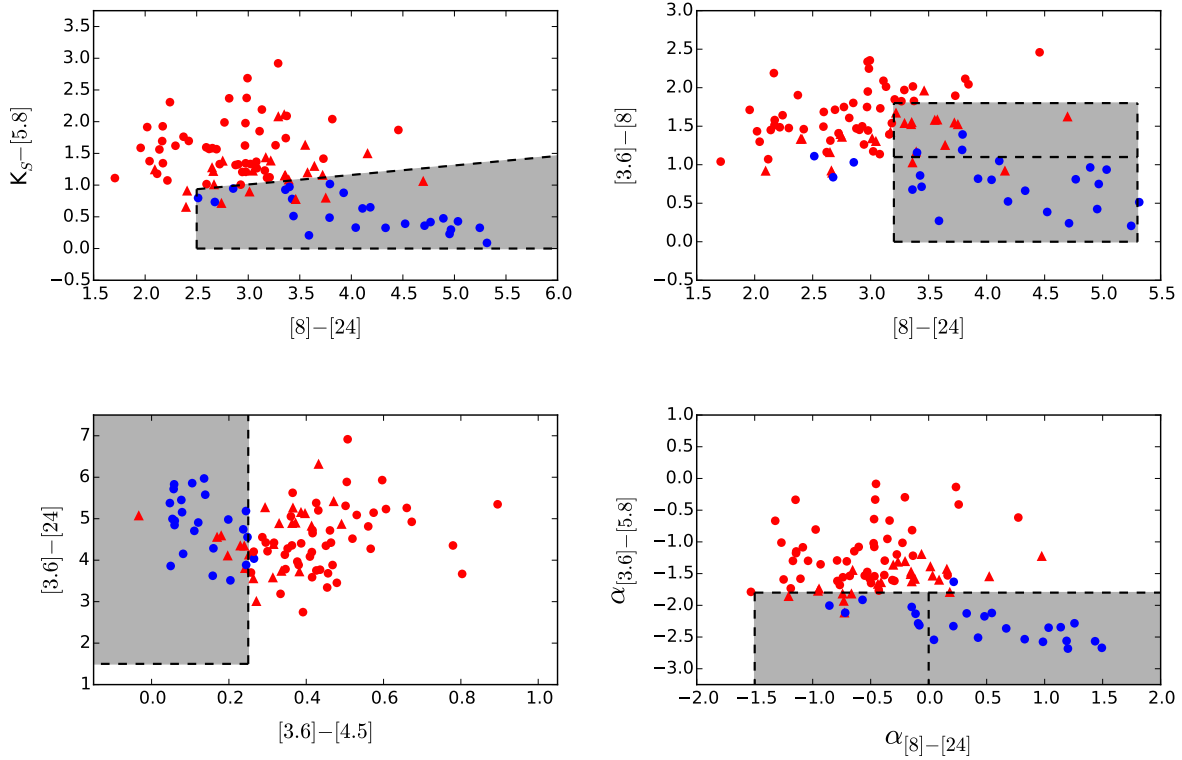


Fig. 6.—: Transitional disk selection criteria (gray shaded area) from Fang et al. (2009, 2013, top left), Merín et al. (2010, top right; Region A is bottom box, Region B is top box), Cieza et al. (2010, bottom left), and Muzerolle et al. (2010, bottom right; weak-excess sources in left box, classical TDs in right box) applied to our L1641 sample (points). Colors and indices utilize 2MASS and *Spitzer* photometry. In this work we identify a protoplanetary disk as transitional (blue circle) if it meets three of the four selection criteria. Red triangles are used to mark candidate transitional disks, objects that meet one or two of the four selection criteria. Full disks are denoted with red circles.

TABLE 3
TRANSITIONAL DISK CANDIDATES

M12 Num	Fang et al. (2009, 2013)	Merín et al. (2010)	Cieza et al. (2010)	Muzerolle et al. (2010)	This work
198	×	×	×	×	×
227	×	×	×	×	×
231		×	×		
232		×			
250	×	×	×	×	×
263	×	×	×	×	×
269	×	×	×	×	×
278	×	×	×	×	×
282		×			
291	×	×			
296	×	×	×	×	×
307	×	×	×	×	×
313			×	×	
342	×		×		
387	×	×	×	×	×
400	×	×			
402		×	×		
403	×		×	×	×
463	×	×	×	×	×
468			×		
483				×	
485	×		×	×	×
487	×	×	×	×	×
488				×	
491	×			×	
556	×	×	×	×	×
561	×				
597		×			
598	×				
619	×		×	×	×
633	×	×	×	×	×
644	×				
666				×	
689	×	×		×	×
751	×	×	×	×	×
761		×			
811	×	×	×		×
818	×	×	×	×	×
832		×			
874			×		
920	×	×	×	×	×

TABLE 3—*Continued*

M12 Num	Fang et al. (2009, 2013)	Merín et al. (2010)	Cieza et al. (2010)	Muzerolle et al. (2010)	This work
926		×			
930		×			
971	×		×	×	×
994		×			
1006	×	×	×	×	×
1011			×		
1020		×			
1086	×	×	×	×	×

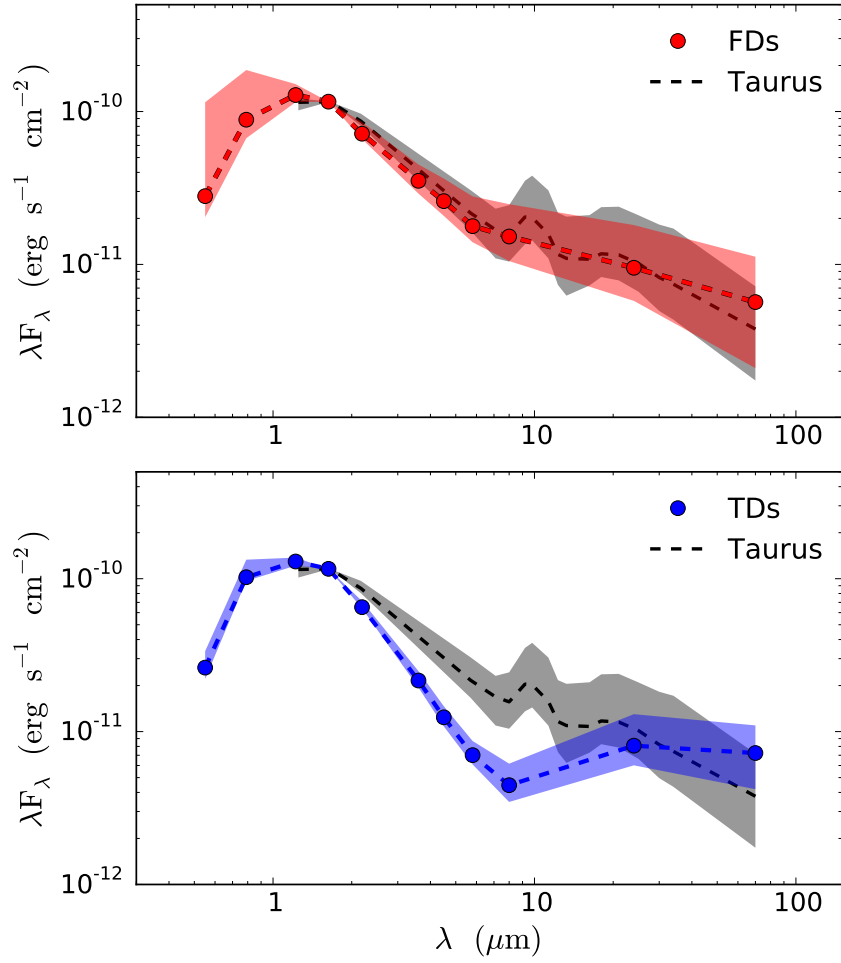


Fig. 7.—: Top: The median SED for full disks (FDs) in the L1641 sample with A_V determinations (red points and dashed line) compared to the Taurus median from Furlan et al. (2006) and extended here to $70 \mu\text{m}$ using data from Howard et al. (2013, black dashed line). Quartiles are shown as the shaded regions. Bottom: The median SED for the transitional disks (TDs) in the L1641 sample (blue points and dashed line) compared to the Taurus median (black dashed line). Quartiles are shown as the shaded regions.

TABLE 4
L1641 MEDIAN SED

Wavelength (μm)	Median ($\log_{10}[\lambda F_{\lambda}]$)	Lower Quartile ($\log_{10}[\lambda F_{\lambda}]$)	Upper Quartile ($\log_{10}[\lambda F_{\lambda}]$)
0.55	-10.567	-10.663	-10.252
0.79	-10.006	-10.121	-9.838
1.22	-9.891	-9.928	-9.824
1.63	-9.935	-9.935	-9.935
2.19	-10.150	-10.189	-10.103
3.6	-10.487	-10.641	-10.378
4.5	-10.655	-10.805	-10.486
5.8	-10.817	-10.974	-10.616
8.0	-10.917	-11.160	-10.662
24.0	-11.054	-11.239	-10.836
70.0	-11.230	-11.619	-10.950

TABLE 5
L1641 MEDIAN SED FOR FULL DISKS

Wavelength (μm)	Median ($\log_{10}[\lambda F_{\lambda}]$)	Lower Quartile ($\log_{10}[\lambda F_{\lambda}]$)	Upper Quartile ($\log_{10}[\lambda F_{\lambda}]$)
0.55	-10.554	-10.691	-9.939
0.79	-10.053	-10.175	-9.728
1.22	-9.892	-9.939	-9.821
1.63	-9.935	-9.935	-9.935
2.19	-10.145	-10.179	-10.069
3.6	-10.453	-10.537	-10.346
4.5	-10.586	-10.682	-10.438
5.8	-10.750	-10.855	-10.555
8.0	-10.817	-10.978	-10.606
24.0	-11.022	-11.239	-10.743
70.0	-11.246	-11.679	-10.950

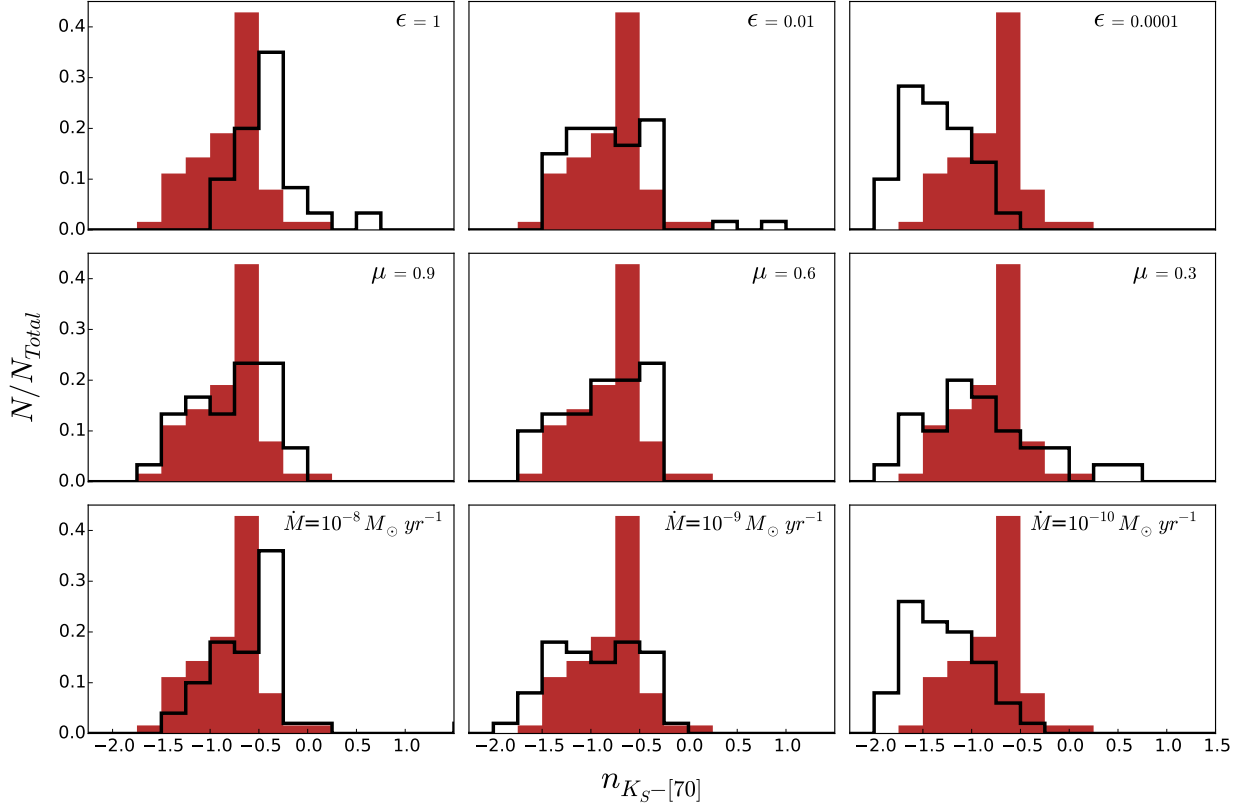


Fig. 8.—: Comparison of the observed $n_{K_S-[70]}$ of L1641 FDs (red) to synthetic $n_{K_S-[70]}$ from the disk model grid (black outline) described in Section 4.1. Each panel shows the $n_{K_S-[70]}$ of models corresponding to the dust settling, inclination, or accretion rate noted in the upper right corner, letting the other parameters vary over the chosen grid range. Each distribution has been normalized by the total number in that sample.

TABLE 6
L1641 MEDIAN SED FOR TRANSITIONAL DISKS

Wavelength (μm)	Median ($\log_{10}[\lambda F_\lambda]$)	Lower Quartile ($\log_{10}[\lambda F_\lambda]$)	Upper Quartile ($\log_{10}[\lambda F_\lambda]$)
0.55	-10.582	-10.656	-10.474
0.79	-9.990	-10.015	-9.876
1.22	-9.887	-9.915	-9.862
1.63	-9.935	-9.935	-9.935
2.19	-10.186	-10.194	-10.147
3.6	-10.666	-10.712	-10.605
4.5	-10.907	-10.966	-10.834
5.8	-11.154	-11.215	-11.062
8.0	-11.351	-11.460	-11.210
24.0	-11.092	-11.221	-10.886
70.0	-11.140	-11.377	-10.960

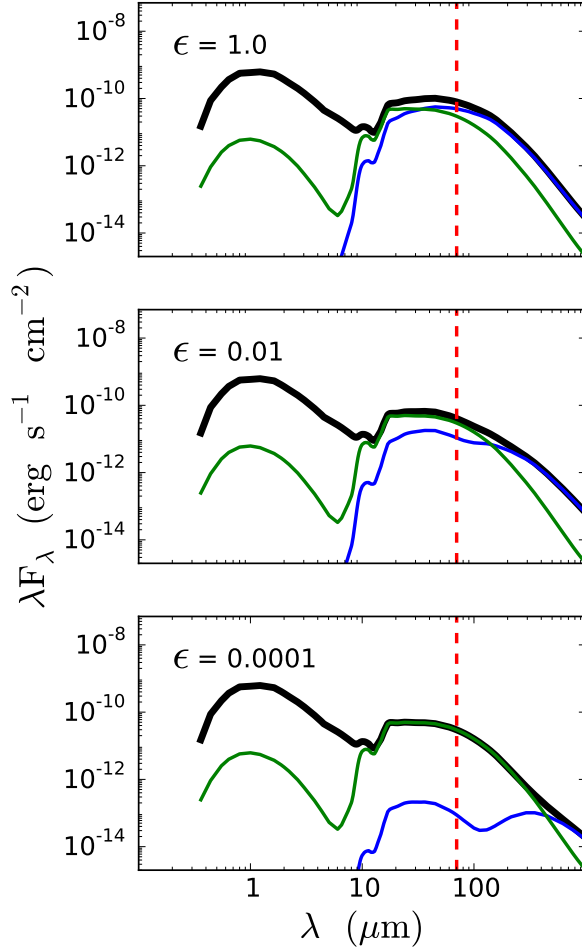


Fig. 9.—: Transitional disk models with varying degrees of settling. The total model (black) includes the photosphere (not shown) and the total disk emission which is composed of emission from the wall (green) and the outer disk (blue). This model has a wall temperature of 150 K and a gap size of ~ 13 AU. Even for moderate settling, the wall emission dominates the flux at $70 \mu\text{m}$ (red dashed line).

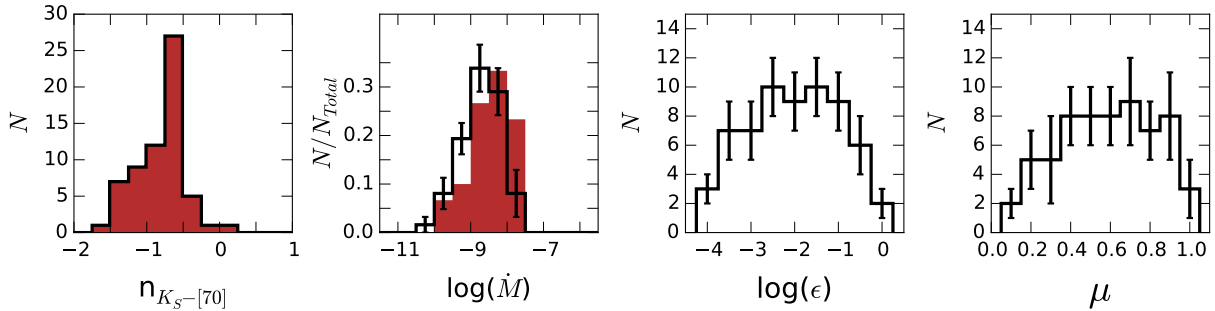


Fig. 10.—: Statistical analysis results for the L1641 FD sample. We show the distributions for observed (red) and predicted (outline) distributions of $n_{K_S-[70]}$, mass accretion rate, dust settling, and inclination ($\mu = \cos(i)$). Error bars are standard deviations of the forward-modeling realizations.

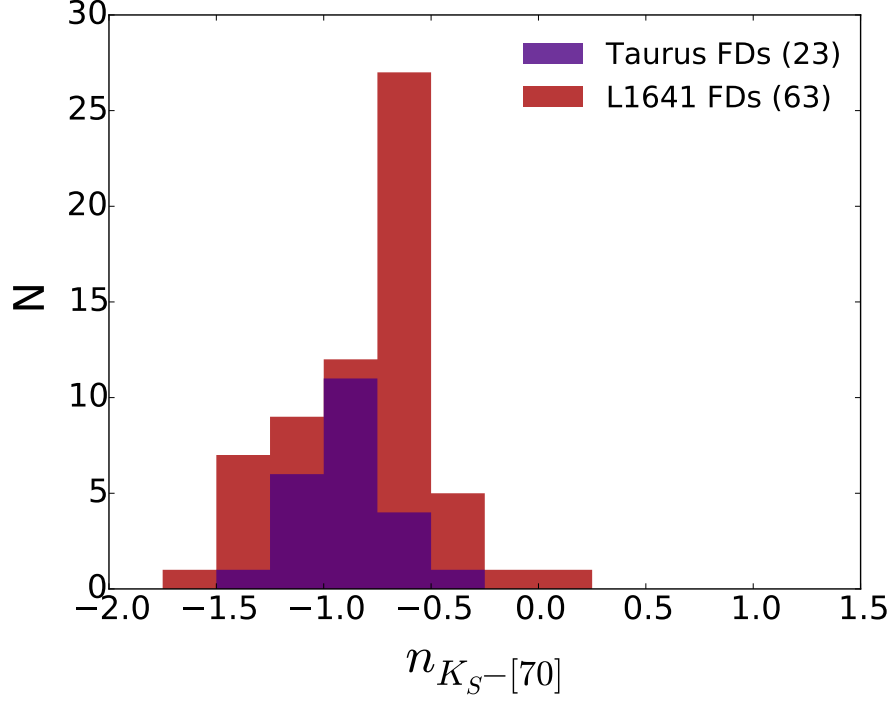


Fig. 11.—: The distribution of the $n_{K_S-[70]}$ index for L1641 FDs (red) and Taurus FDs (purple).

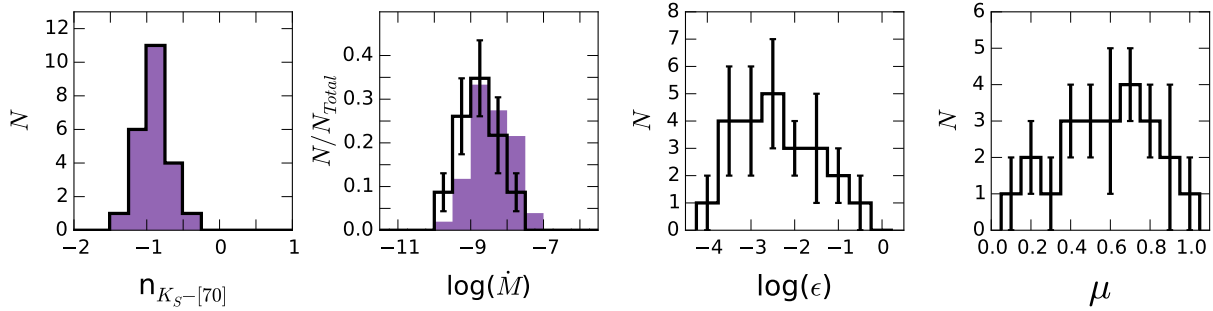


Fig. 12.—: Statistical analysis results for the Taurus FD sample. We show the distributions for observed (purple) and predicted (outline) distributions of $n_{K_S-[70]}$, mass accretion rate, dust settling, and inclination ($\mu = \cos(i)$). Error bars are standard deviations of the forward-modeling realizations.

TABLE 7
Herschel FLUXES FOR FLAGGED OBJECTS

M12 Num	RA(J2000)	Dec(J2000)	F ₇₀ (Jy)	Flag
206	05:43:00.9	-08:44:18.4	0.235±0.012	2
229	05:41:22.6	-08:39:16.0	0.155±0.008	1
230	05:41:22.9	-08:39:11.0	0.173±0.009	1
236	05:42:48.7	-08:38:30.8	0.449±0.023	1
237	05:42:50.5	-08:38:29.1	0.171±0.009	1
239	05:42:49.7	-08:38:25.7	0.091±0.006	1
241	05:42:47.4	-08:38:08.6	0.131±0.007	1
259	05:42:50.3	-08:34:37.6	0.057±0.004	2
286	05:42:49.4	-08:17:07.2	0.113±0.007	1
300	05:40:20.9	-08:14:06.4	0.63±0.03	1
328	05:42:44.0	-08:09:26.7	0.053±0.004	1
349	05:40:44.2	-08:07:34.8	0.205±0.011	1
350	05:40:25.0	-08:07:33.0	0.508±0.026	1
351	05:40:46.6	-08:07:12.9	0.84±0.04	1
364	05:40:48.0	-08:05:58.7	3.77±0.19	1
371	05:40:46.2	-08:05:24.5	0.80±0.04	1
376	05:40:46.8	-08:04:54.6	0.048±0.003	1
421	05:40:20.5	-07:56:39.6	2.90±0.15	1
431	05:41:20.1	-07:55:23.8	0.143±0.008	1
438	05:41:30.0	-07:54:21.1	0.0431±0.0027	2
448	05:41:21.7	-07:53:16.3	0.054±0.003	2
467	05:41:22.7	-07:49:16.1	0.0413±0.0027	2
478	05:40:58.9	-07:48:01.5	0.0378±0.0026	1
479	05:40:38.5	-07:47:46.8	0.104±0.006	2
510	05:40:31.3	-07:37:01.2	0.052±0.003	2
523	05:39:53.5	-07:30:09.5	0.85±0.05	1,2
526	05:39:55.1	-07:29:37.0	0.166±0.022	1
533	05:39:54.7	-07:27:44.1	0.193±0.010	2
534	05:40:08.0	-07:27:41.2	0.160±0.008	1
535	05:40:10.3	-07:27:38.2	0.576±0.029	1
540	05:39:22.3	-07:26:44.5	3.88±0.19	1
541	05:39:58.1	-07:26:41.2	0.062±0.004	2
571	05:39:48.4	-07:24:14.9	0.270±0.014	2
576	05:39:42.5	-07:23:16.5	0.051±0.003	2
586	05:38:52.4	-07:21:09.4	1.01±0.05	1
590	05:39:28.6	-07:20:31.1	0.266±0.014	2
612	05:38:58.6	-07:16:45.7	8.1±0.4	1
634	05:39:09.5	-07:09:17.7	0.086±0.005	2
643	05:39:00.6	-07:06:30.0	0.105±0.006	2
648	05:39:05.2	-07:05:42.0	0.038±0.003	2
676	05:38:45.7	-07:01:58.5	0.69±0.03	1,2

TABLE 7—*Continued*

M12 Num	RA(J2000)	Dec(J2000)	F ₇₀ (Jy)	Flag
679	05:38:47.2	-07:01:53.4	0.341±0.017	1
686	05:38:21.2	-07:01:20.5	0.045±0.004	1
712	05:38:40.1	-06:59:14.6	0.107±0.006	1
720	05:38:43.8	-06:58:22.3	0.388±0.020	1
725	05:38:44.9	-06:58:14.6	0.108±0.007	1
726	05:38:43.2	-06:58:08.9	2.89±0.15	1
760	05:38:09.3	-06:49:16.8	3.34±0.17	1
776	05:36:21.4	-06:45:36.8	1.91±0.10	1
782	05:36:05.0	-06:44:42.9	0.137±0.015	1,2
786	05:36:33.0	-06:44:29.3	0.177±0.010	1
788	05:36:32.9	-06:44:21.0	0.158±0.009	1
796	05:36:25.4	-06:42:57.4	10.1±0.6	1
804	05:37:47.0	-06:42:30.2	1.13±0.06	3
812	05:36:32.4	-06:40:42.9	0.103±0.008	1
827	05:35:58.2	-06:36:42.9	0.028±0.006	1
838	05:37:13.2	-06:35:00.6	0.288±0.015	1
886	05:36:21.8	-06:26:01.9	0.036±0.006	1
918	05:36:12.9	-06:23:30.6	0.280±0.015	1
925	05:36:23.8	-06:23:11.1	0.543±0.028	1
927	05:36:21.5	-06:22:52.4	0.402±0.021	1
939	05:36:11.4	-06:22:22.1	0.093±0.005	1
950	05:36:21.0	-06:21:53.1	1.03±0.06	1,2
960	05:36:18.5	-06:20:38.7	0.057±0.007	1
1065	05:35:34.6	-06:02:47.1	0.131±0.008	1

NOTE.—For each object, we list the corresponding identification number from Megeath et al. (2012) and the objects associated flag. A flag of “1” denotes a protoplanetary system with a 70 μm flux that is likely contaminated by close sources and/or nebulosity; “2” identifies systems with $A_V \geq 15$; “3” labels systems that do not have colors characteristic of CTTSs. These sources are not included in our analysis

TABLE 8
STELLAR PROPERTIES FOR FLAGGED OBJECTS

M12 Num	SpT	SpT Ref.	A_V	A_V Ref.	L (L_\odot)	L Ref.	$\log \dot{M}$ ($M_\odot \text{ yr}^{-1}$)	\dot{M} Ref.	Flag
206			22.87	CTTS J-H					2
229			3.41	CTTS J-H					1
230	M1.8	a	2.9	c	0.773	c	-7.8	c	1
236	K7.5	a	4	c	3.748	c	-6.8	c	1
237			14.91	CTTS J-H					1
239			14.51	CTTS J-H					1
241			10.55	CTTS J-H					1
259			19.9	b	1.72	b			2
328	M0.0	a	5.2	c	0.79	c	< -8.7	c	1
349			8.77	CTTS J-H					1
350	G4.0	a	2	b	5.5	b	-7.13	a	1
351	K7.0	c	8.58	b	7.19	b	< -8.19	b	1
364	K5.0	c	2.4	c	7.394	c	< -8	c	1
371	K3.0	a	3.09	b	8.18	b	-7.86	b	1
376	M2.5	d	5.2	d	1.231	d			1
421			12.3	b	9.19	b			1
431	M4.0	d	10.2	d	0.581	d	-8.23	d	1
438			16.11	CTTS J-H					2
448			27.27	CTTS J-H					2
467			17.6	b	1.22	b			2
478			2.75	b	0.11	b			1
479			22	b	4.13	b			2
510			15.47	CTTS J-H					2
523			21.5	b	1.75	b			1,2
533			34.5	b	53.61	b			2
535	K7.0	b	9.96	b	4.6	b			1
540	K7.0	a	6	c	19.795	c	-5.6	c	1
541			22	b	3.14	b			2
571			19.3	b	1.99	b			2
576			15.7	b	1.81	b			2
586	G4.5	a	4.6	c	10.504	c	-6.8	c	1
590			20.4	b	0.66	b			2
612	A9.0	e	0.0	CTTS J-H					1
634			21.87	CTTS J-H					2
643			21.5	CTTS J-H					2
648			15.04	CTTS J-H					2
676			26.79	CTTS J-H					1,2
686	M4.5	a	1.4	d	0.102	d	-9.78	d	1
712	M0.5	a	3.7	b	0.68	b	-7.7	c	1
720	K7.5	a	4.5	d	0.359	d	-8.83	d	1
725	K7.5	a	8.42	b	1.89	b	-7.64	d	1

TABLE 8—*Continued*

M12 Num	SpT	SpT Ref.	A_V	A_V Ref.	L (L_\odot)	L Ref.	$\log \dot{M}$ ($M_\odot \text{ yr}^{-1}$)	\dot{M} Ref.	Flag
726	K7.5	d	11.3	b	14.57	b			1
760	A3.5	b	3.58	b	34.38	b	-7.9	b	1
776	K5.0	a	5.92	b	9.09	b	< -7.46	b	1
782			15.2	CTTS J-H					1,2
786			8.35	CTTS J-H					1
788	M2.0	a	3.74	b	0.55	b	-7.99	d	1
796			0.56	CTTS J-H					1
804	A1.0	e							3
812	M4.5	a	0	c	0.166	c	-9.45	c	1
827	K7.5	a	1.55	b	1.06	b	-8.31	b	1
838	A7.0	a	0.83	b	27.41	b	-7.15	b	1
886	K7.4	a	3.6	c	1.066	c	-7.9	c	1
918	M1.5	a	1.37	b	1.19	b			1
925			12.2	b	2.15	b			1
927	M0.5	d	9.5	d	0.636	d	-7.75	d	1
939	M0.0	a	6.3	d	1.436	d	-7.76	d	1
950			15.89	CTTS J-H					1,2
960	M0.5	a	0.6	d	0.533	d	-8.16	d	1
1065	M1.5	a	9.79	CTTS J-H					1

NOTE.—References: ^aHsu et al. (2012), ^bKim et al. (2016), ^cFang et al. (2013), ^dFang et al. (2009), ^eHsu et al. (2013). For sources with an A_V reference of CTTS J-H, visual extinctions were measured in this work as described in Section 3.1. Flags are the same as noted in Table 7. Flagged objects are not included in our analysis

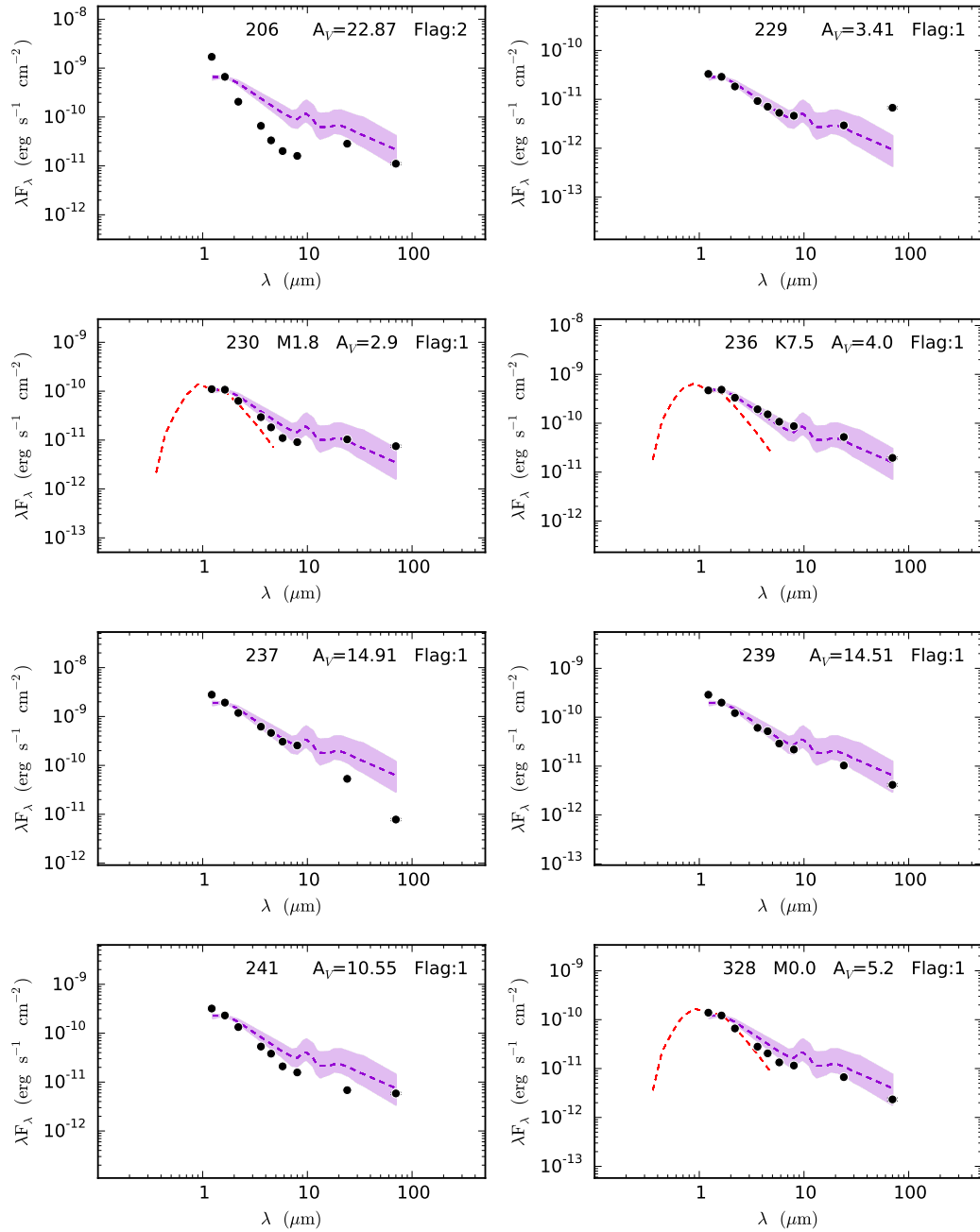


Fig. 13.— SEDs for the L1641 sources that are flagged and not included in our analysis. Flags are the same as noted in Table 7.

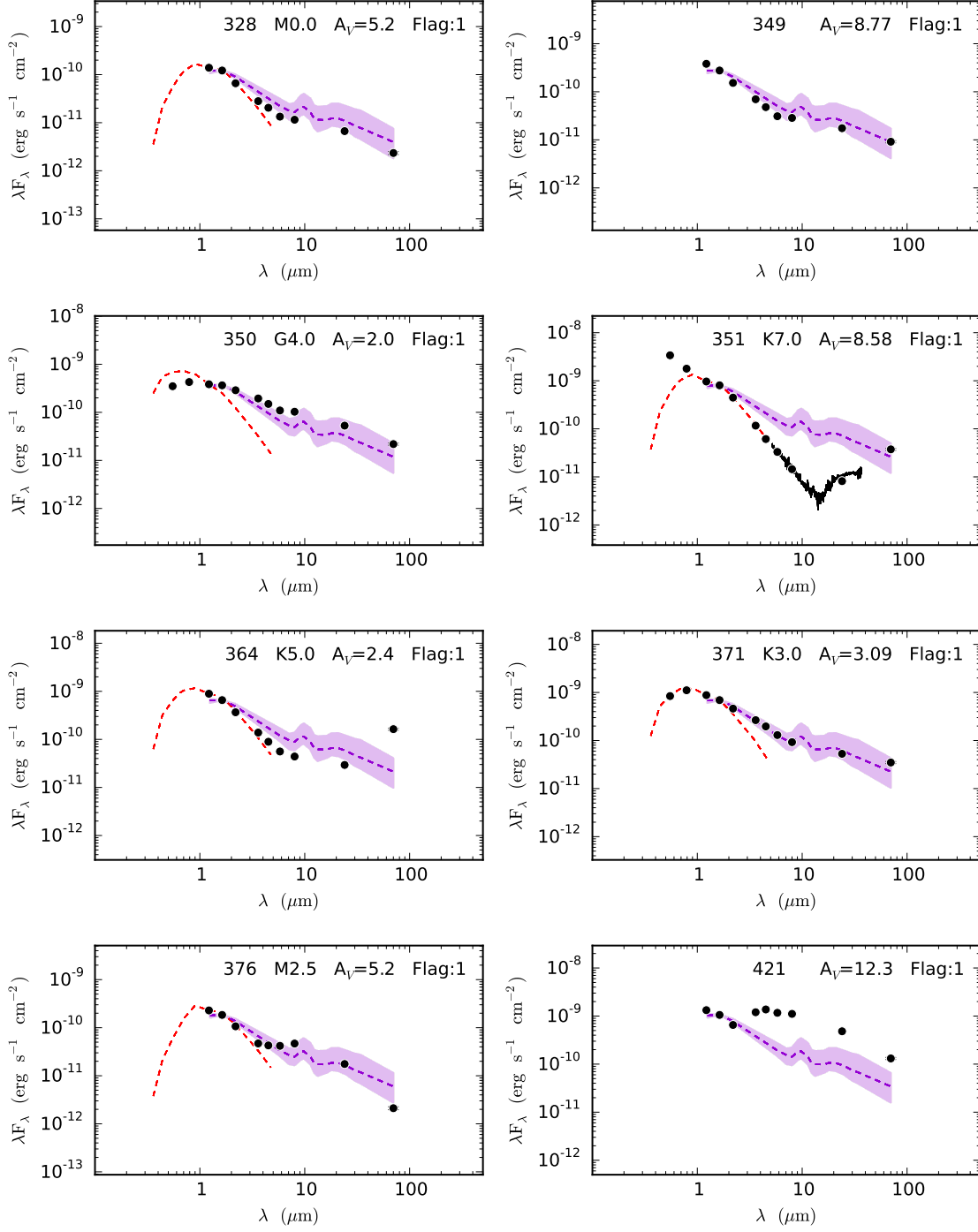


Fig. 13.—: Continued

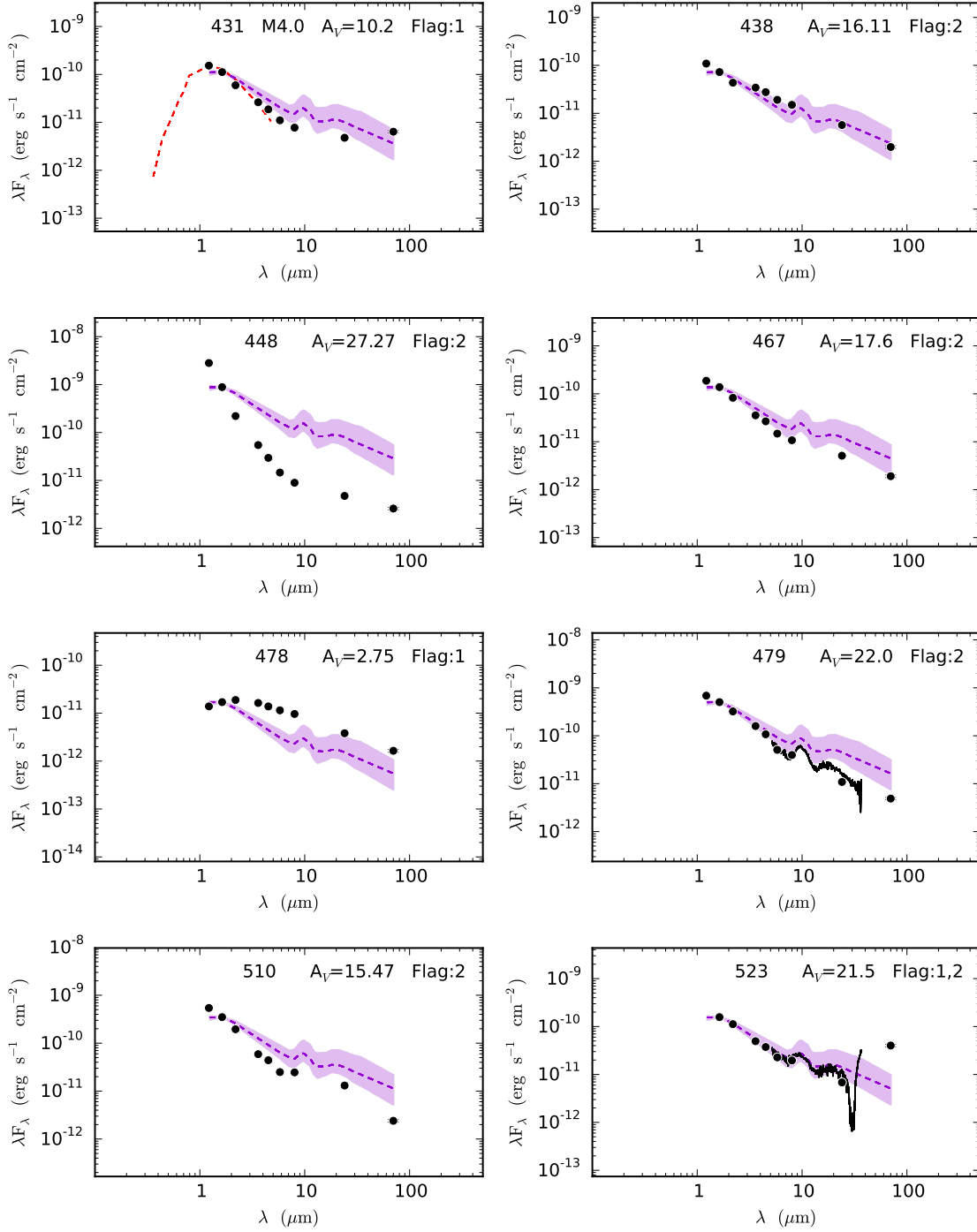


Fig. 13.—: Continued

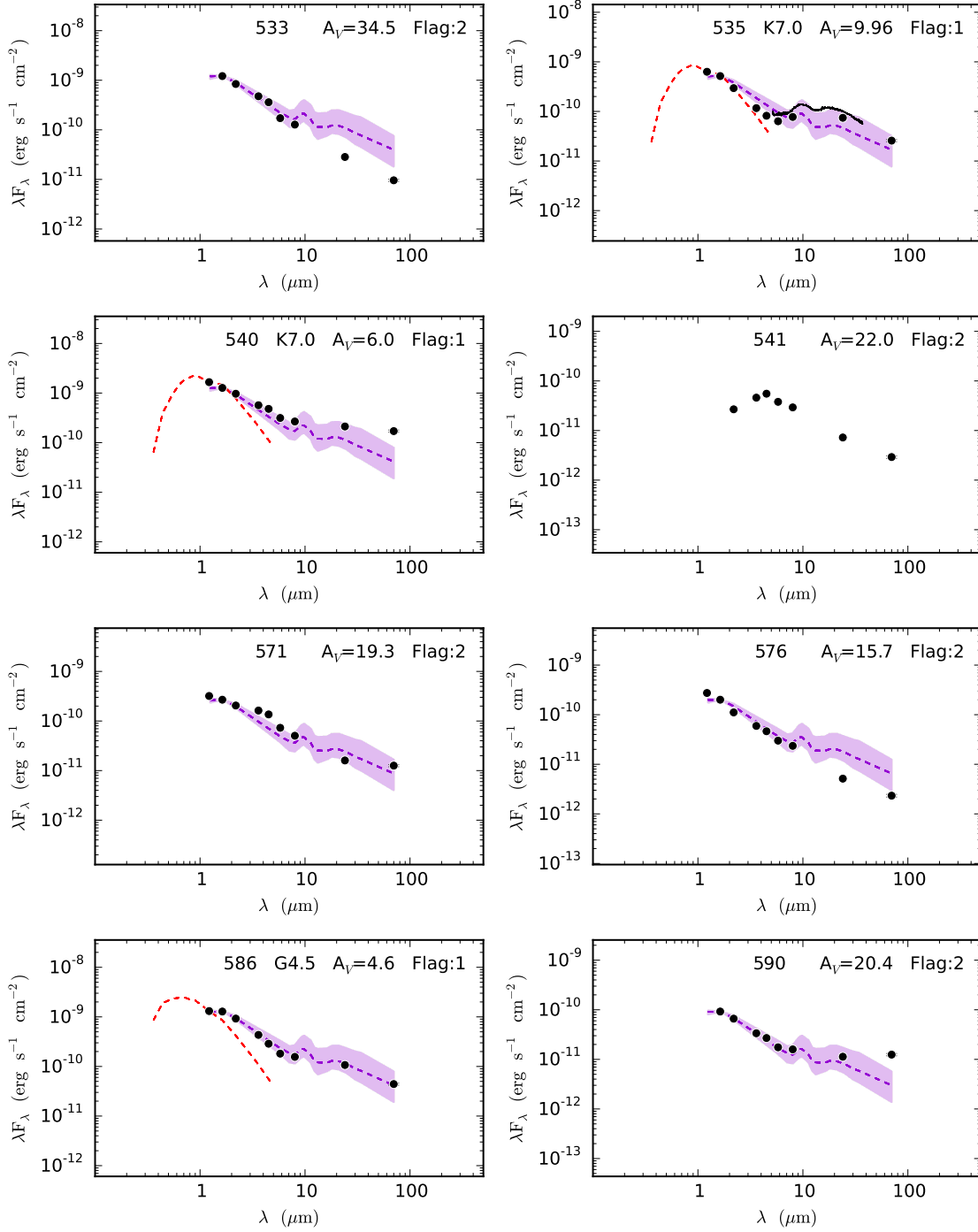


Fig. 13.—: Continued

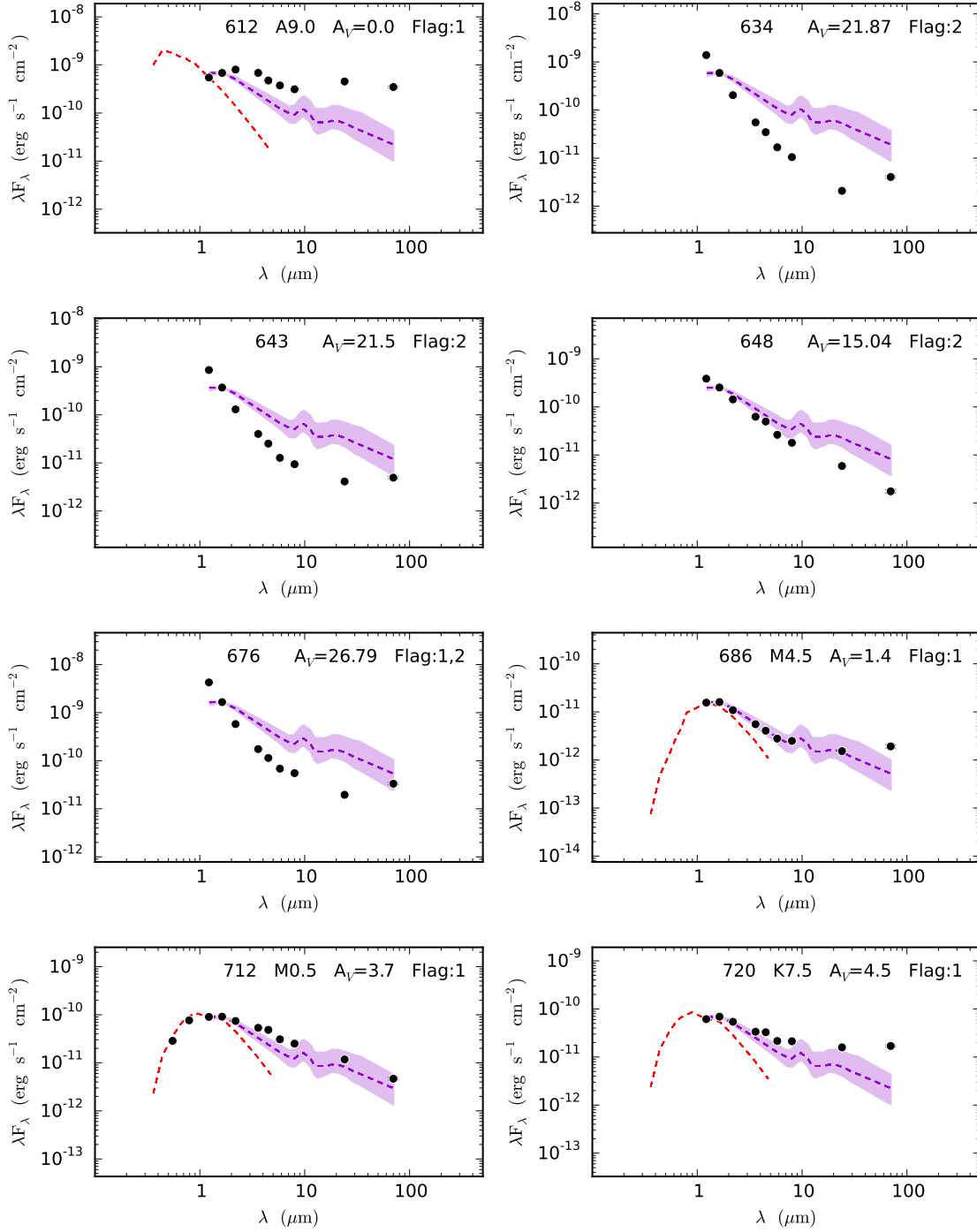


Fig. 13.—: Continued

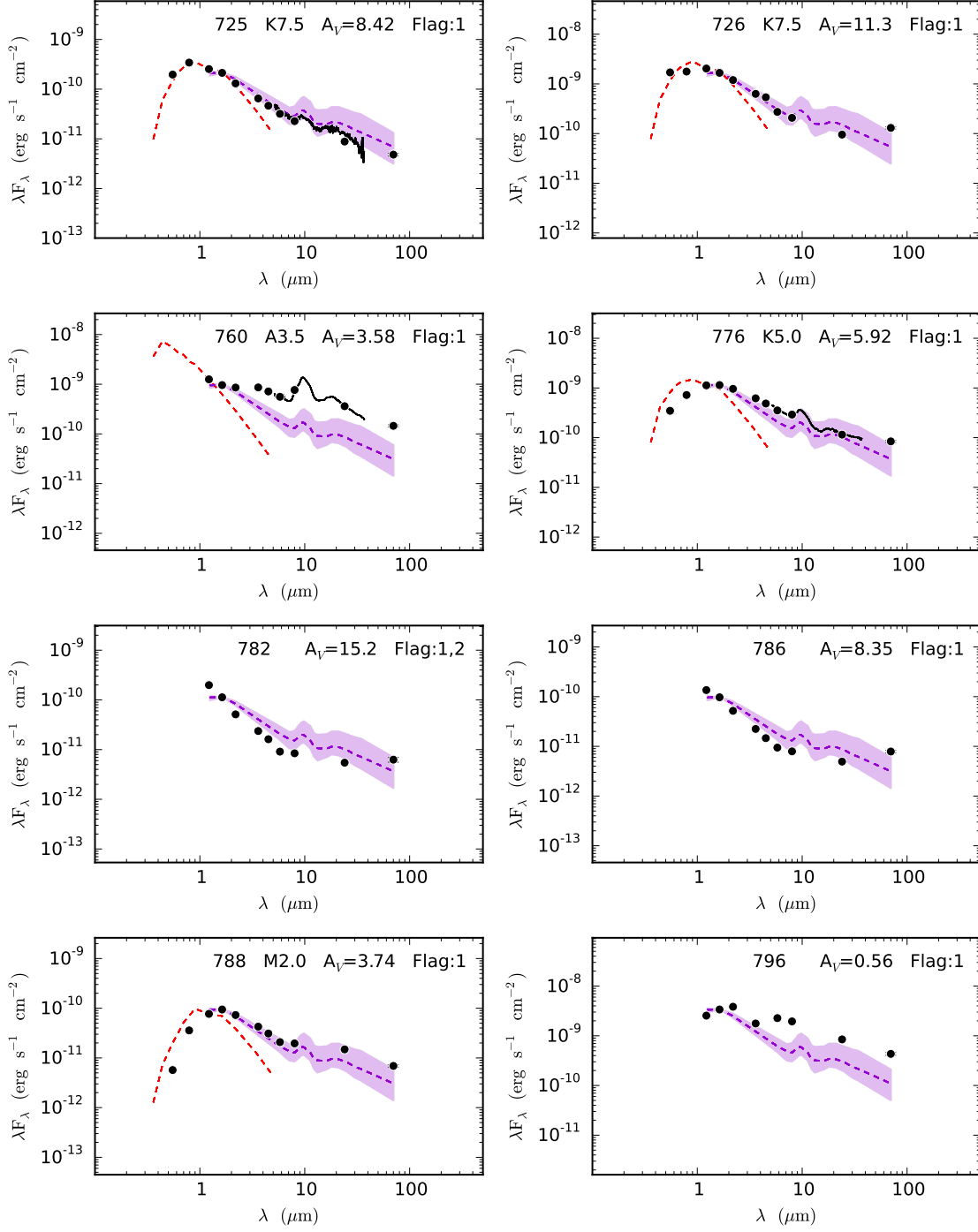


Fig. 13.—: Continued

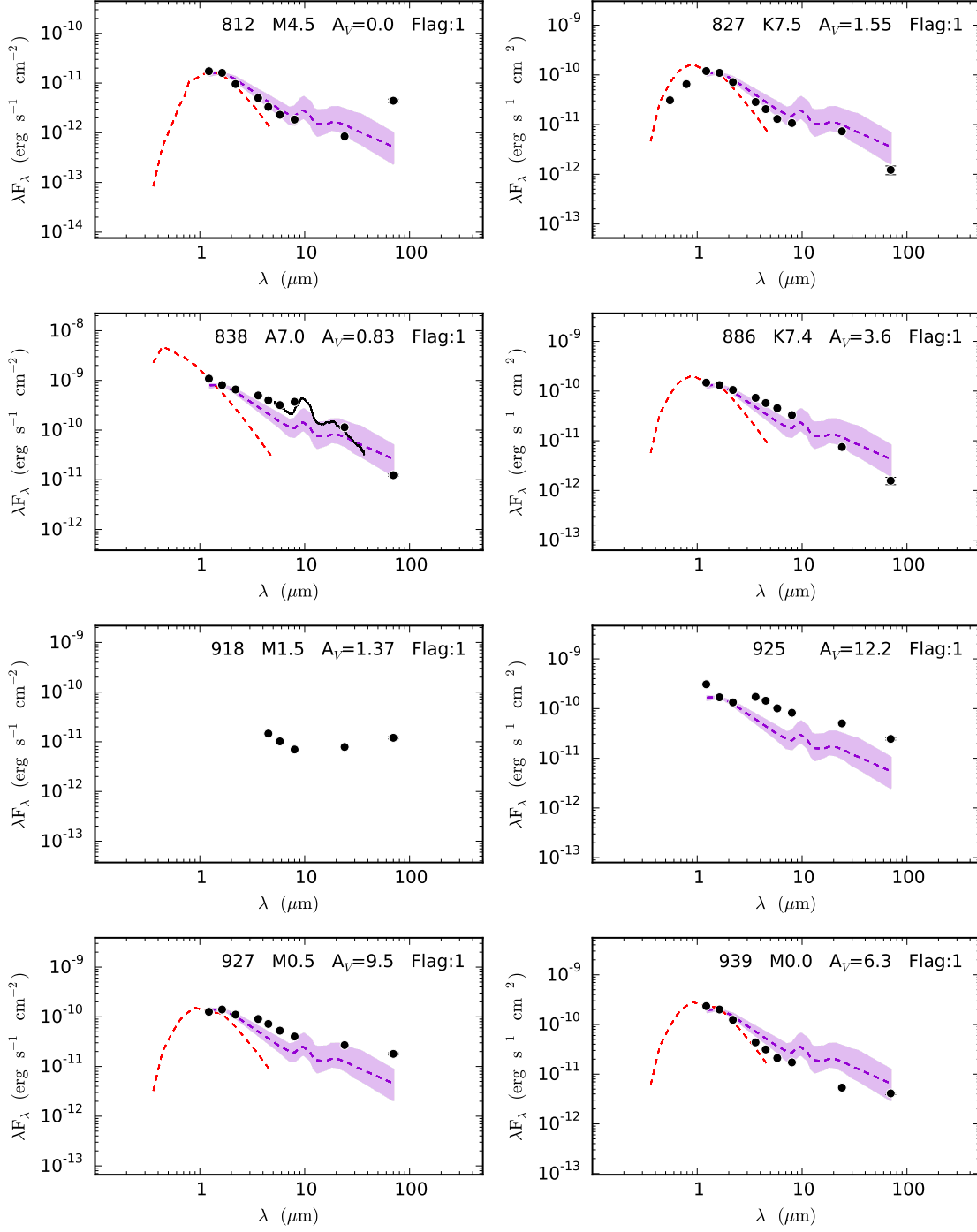


Fig. 13.—: Continued

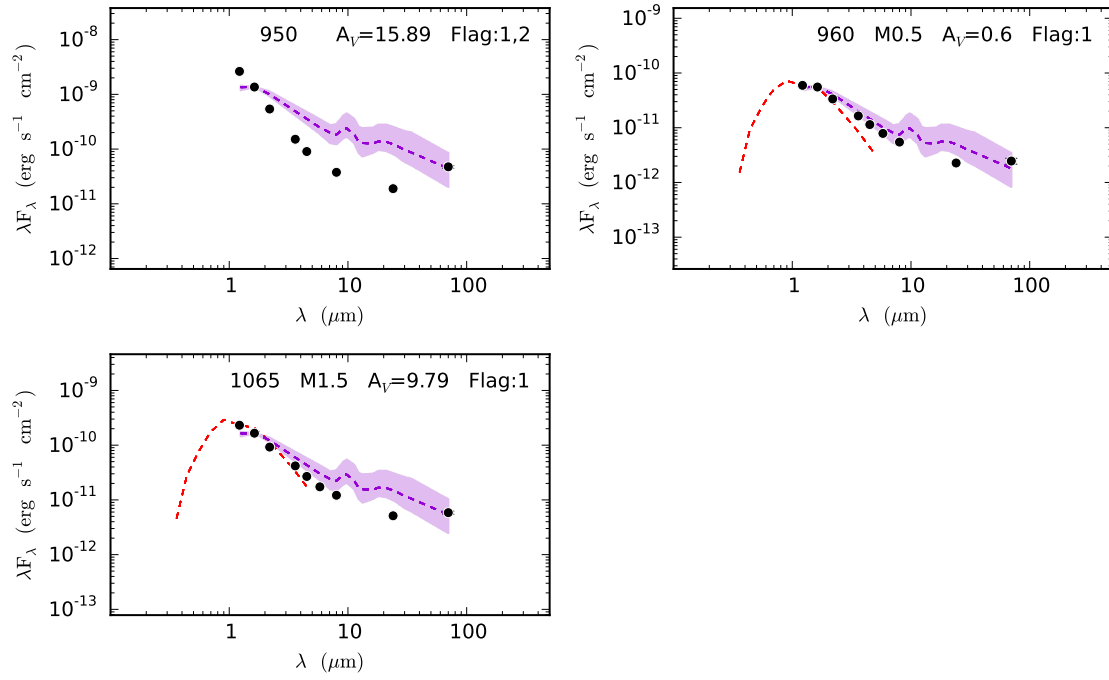


Fig. 13.—: Continued

REFERENCES

- Adams, F. C., Lada, C. J., & Shu, F. H. 1987, *ApJ*, 312, 788
- Alexander, R., Pascucci, I., Andrews, S., Armitage, P., & Cieza, L. 2014, *Protostars and Planets VI*, 475
- Andre, P., & Montmerle, T. 1994, *ApJ*, 420, 837
- Andrews, S. M., Rosenfeld, K. A., Kraus, A. L., & Wilner, D. J. 2013, *ApJ*, 771, 129
- Armitage, P. J. 2018, *ArXiv e-prints*, arXiv:1803.10526
- Baraffe, I., Chabrier, G., Allard, F., & Hauschildt, P. H. 1998, *A&A*, 337, 403
- Bessell, M. S., & Brett, J. M. 1988, *PASP*, 100, 1134
- Bustamante, I., Merín, B., Ribas, Á., et al. 2015, *A&A*, 578, A23
- Calvet, N., & Gullbring, E. 1998, *ApJ*, 509, 802
- Calvet, N., Hartmann, L., Kenyon, S. J., & Whitney, B. A. 1994, *ApJ*, 434, 330
- Calvet, N., Magris, G. C., Patino, A., & D'Alessio, P. 1992, *Revista Mexicana de Astronomia y Astrofisica*, 24
- Caratti o Garatti, A., Garcia Lopez, R., Antonucci, S., et al. 2012, *A&A*, 538, A64
- Carpenter, J. M. 2001, *AJ*, 121, 2851
- Chiang, E., & Murray-Clay, R. 2007, *Nature Physics*, 3, 604
- Chiang, E. I., & Goldreich, P. 1997, *ApJ*, 490, 368
- Ciesla, F. J. 2007, *ApJ*, 654, L159
- Cieza, L. A., Schreiber, M. R., Romero, G. A., et al. 2010, *ApJ*, 712, 925
- Clarke, C. J., Gendrin, A., & Sotomayor, M. 2001, *MNRAS*, 328, 485
- D'Alessio, P., Calvet, N., & Hartmann, L. 2001, *ApJ*, 553, 321
- D'Alessio, P., Calvet, N., Hartmann, L., Franco-Hernández, R., & Servín, H. 2006, *ApJ*, 638, 314
- D'Alessio, P., Calvet, N., Hartmann, L., Lizano, S., & Cantó, J. 1999, *ApJ*, 527, 893
- D'Alessio, P., Cantó, J., Calvet, N., & Lizano, S. 1998, *ApJ*, 500, 411
- D'Alessio, P., Hartmann, L., Calvet, N., et al. 2005, *ApJ*, 621, 461
- Dorschner, J., Begemann, B., Henning, T., Jaeger, C., & Mutschke, H. 1995, *A&A*, 300, 503
- Dotter, A., Chaboyer, B., Jevremović, D., et al. 2008, *ApJS*, 178, 89
- Draine, B. T., & Lee, H. M. 1984, *ApJ*, 285, 89
- Dullemond, C. P., & Dominik, C. 2004, *A&A*, 421, 1075
- . 2005, *A&A*, 434, 971
- Dunham, M. M., Stutz, A. M., Allen, L. E., et al. 2014, *Protostars and Planets VI*, 195
- Espaillet, C., Muzerolle, J., Najita, J., et al. 2014, *Protostars and Planets VI*, 497
- Evans, II, N. J., Dunham, M. M., Jørgensen, J. K., et al. 2009, *ApJS*, 181, 321
- Fang, M., Kim, J. S., van Boekel, R., et al. 2013, *ApJS*, 207, 5
- Fang, M., van Boekel, R., Wang, W., et al. 2009, *A&A*, 504, 461
- Fazio, G. G., Hora, J. L., Allen, L. E., et al. 2004, *ApJS*, 154, 10
- Fischer, W., Edwards, S., Hillenbrand, L., & Kwan, J. 2011, *ApJ*, 730, 73
- Fischer, W. J., Megeath, S. T., Furlan, E., et al. 2017, *ApJ*, 840, 69
- Flaherty, K. M., Hughes, A. M., Rosenfeld, K. A., et al. 2015, *ApJ*, 813, 99
- Flaherty, K. M., Hughes, A. M., Rose, S. C., et al. 2017, *ApJ*, 843, 150
- Furlan, E., Hartmann, L., Calvet, N., et al. 2006, *ApJS*, 165, 568

- Furlan, E., Watson, D. M., McClure, M. K., et al. 2009, *ApJ*, 703, 1964
- Furlan, E., Luhman, K. L., Espaillat, C., et al. 2011, *ApJS*, 195, 3
- Furlan, E., Fischer, W. J., Ali, B., et al. 2016, *ApJS*, 224, 5
- Gálfalk, M., & Olofsson, G. 2008, *A&A*, 489, 1409
- Goldreich, P., & Ward, W. R. 1973, *ApJ*, 183, 1051
- Greene, T. P., Wilking, B. A., Andre, P., Young, E. T., & Lada, C. J. 1994, *ApJ*, 434, 614
- Gutermuth, R. A., Myers, P. C., Megeath, S. T., et al. 2008, *ApJ*, 674, 336
- Hartmann, L., Ballesteros-Paredes, J., & Bergin, E. A. 2001, *ApJ*, 562, 852
- Hartmann, L., Calvet, N., Gullbring, E., & D'Alessio, P. 1998, *ApJ*, 495, 385
- Hendler, N. P., Pinilla, P., Pascucci, I., et al. 2018, *MNRAS*, 475, L62
- Hernández, J., Calvet, N., Briceño, C., Hartmann, L., & Berlind, P. 2004, *AJ*, 127, 1682
- Houck, J. R., Roellig, T. L., van Cleve, J., et al. 2004, *ApJS*, 154, 18
- Howard, C. D., Sandell, G., Vacca, W. D., et al. 2013, *ApJ*, 776, 21
- Hsu, W.-H., Hartmann, L., Allen, L., et al. 2012, *ApJ*, 752, 59
- . 2013, *ApJ*, 764, 114
- Ingleby, L., Calvet, N., Bergin, E., et al. 2011, *ApJ*, 743, 105
- Ingleby, L., Calvet, N., Herczeg, G., et al. 2013, *ApJ*, 767, 112
- Kenyon, S. J., & Hartmann, L. 1987, *ApJ*, 323, 714
- . 1995, *ApJS*, 101, 117
- Kim, K. H., Watson, D. M., Manoj, P., et al. 2013, *ApJ*, 769, 149
- . 2016, *ApJS*, 226, 8
- Koenig, X. P., Leisawitz, D. T., Benford, D. J., et al. 2012, *ApJ*, 744, 130
- Kounkel, M., Megeath, S. T., Poteet, C. A., Fischer, W. J., & Hartmann, L. 2016, *ApJ*, 821, 52
- Kounkel, M., Hartmann, L., Loinard, L., et al. 2017, *ApJ*, 834, 142
- Kryukova, E., Megeath, S. T., Hora, J. L., et al. 2014, *AJ*, 148, 11
- Lada, C. J. 1987, in *IAU Symposium*, Vol. 115, *Star Forming Regions*, ed. M. Peimbert & J. Jugaku, 1–17
- Lebouteiller, V., Barry, D. J., Spoon, H. W. W., et al. 2011, *ApJS*, 196, 8
- Lewis, J. A., & Lada, C. J. 2016, *ApJ*, 825, 91
- Lubow, S. H., & D'Angelo, G. 2006, *ApJ*, 641, 526
- Luhman, K. L. 2004, *ApJ*, 602, 816
- Luhman, K. L., Allen, P. R., Espaillat, C., Hartmann, L., & Calvet, N. 2010, *ApJS*, 186, 111
- Luhman, K. L., & Rieke, G. H. 1999, *ApJ*, 525, 440
- Manoj, P., Kim, K. H., Furlan, E., et al. 2011, *ApJS*, 193, 11
- Manoj, P., Watson, D. M., Neufeld, D. A., et al. 2013, *ApJ*, 763, 83
- Marsh, K. A., & Mahoney, M. J. 1992, *ApJ*, 395, L115
- Mathis, J. S. 1990, *ARA&A*, 28, 37
- Maucó, K., Hernández, J., Calvet, N., et al. 2016, *ApJ*, 829, 38
- McClure, M. 2009, *ApJ*, 693, L81
- McClure, M. K., Furlan, E., Manoj, P., et al. 2010, *ApJS*, 188, 75
- McClure, M. K., Calvet, N., Espaillat, C., et al. 2013a, *ApJ*, 769, 73
- McClure, M. K., D'Alessio, P., Calvet, N., et al. 2013b, *ApJ*, 775, 114

- Megeath, S. T., Gutermuth, R., Muzerolle, J., et al. 2012, *AJ*, 144, 192
- . 2016, *AJ*, 151, 5
- Merín, B., Brown, J. M., Oliveira, I., et al. 2010, *ApJ*, 718, 1200
- Meyer, M. R., Calvet, N., & Hillenbrand, L. A. 1997, *AJ*, 114, 288
- Muzerolle, J., Allen, L. E., Megeath, S. T., Hernández, J., & Gutermuth, R. A. 2010, *ApJ*, 708, 1107
- Pilbratt, G. L., Riedinger, J. R., Passvogel, T., et al. 2010, *A&A*, 518, L1
- Pillitteri, I., Wolk, S. J., Megeath, S. T., et al. 2013, *ApJ*, 768, 99
- Pinilla, P., Pérez, L. M., Andrews, S., et al. 2017, *ApJ*, 839, 99
- Poglitsch, A., Waelkens, C., Geis, N., et al. 2010, *A&A*, 518, L2
- Rayner, J. T., Toomey, D. W., Onaka, P. M., et al. 2003, *PASP*, 115, 362
- Rebollido, I., Merín, B., Ribas, Á., et al. 2015, *A&A*, 581, A30
- Ribas, Á., Merín, B., Bouy, H., et al. 2013, *A&A*, 552, A115
- Rieke, G. H., Young, E. T., Engelbracht, C. W., et al. 2004, *ApJS*, 154, 25
- Rosotti, G. P., Juhasz, A., Booth, R. A., & Clarke, C. J. 2016, *MNRAS*, 459, 2790
- Shakura, N. I., & Sunyaev, R. A. 1973, *A&A*, 24, 337
- Siess, L., Dufour, E., & Forestini, M. 2000, *A&A*, 358, 593
- Skrutskie, M. F., Cutri, R. M., Stiening, R., et al. 2006, *AJ*, 131, 1163
- Stutz, A. M., & Gould, A. 2016, *A&A*, 590, A2
- Stutz, A. M., & Kainulainen, J. 2015, *A&A*, 577, L6
- Stutz, A. M., Tobin, J. J., Stanke, T., et al. 2013, *ApJ*, 767, 36
- Takeuchi, T., & Lin, D. N. C. 2002, *ApJ*, 581, 1344
- Terebey, S., Shu, F. H., & Cassen, P. 1984, *ApJ*, 286, 529
- Testi, L., Birnstiel, T., Ricci, L., et al. 2014, *Protostars and Planets VI*, 339
- van der Marel, N., Williams, J. P., Ansdell, M., et al. 2018, *ApJ*, 854, 177
- Weidenschilling, S. J. 1980, *Icarus*, 44, 172
- White, R. J., & Ghez, A. M. 2001, *ApJ*, 556, 265
- Wright, E. L., Eisenhardt, P. R. M., Mainzer, A. K., et al. 2010, *AJ*, 140, 1868